FACULTE DES SCIENCES

Jülich Centre for Neutron Science JCNS und Peter Grünberg Institut PGI

JCNS-2, PGI-4: Scattering Methods

"Lattice Dynamics in Emerging Functional Materials" group

Forschungszentrum Jülich

Lattice dynamics in thermoelectric Zintl phases

Année académique 2010–2011

Dissertation présentée par
Anne Möchel
en vue de l'obtention du grade de
Docteur en Sciences

Acknowledgements

My very first gratitude goes to Dr. Raphaël P. Hermann for advising and supporting me during my doctoral thesis and for the fruitful discussions.

My special thanks go to my co-supervisor Dr. Werner Schweika, for his suggestions and especially for his comments on and the correction of this dissertation.

I would also like to thank my co-advisor at the University Liège Prof. R. Cloots. I thank Prof. J.-P. Gaspard and Dr. W. Schweika for accepting to be in my thesis advisory comittee and Prof. B. Vertruyen, Prof. M. Verstraete and Dr. Ilya Sergueev for accepting to be members of the examination jury.

Many people collaborated to this work and I would like to specially thank Mr. D. Bessas, Dr. S. Disch, Dr. A. Houben, Dr. F. Juranyi, Dr. D. Robinson, Dr. K. Schmalzl, Dr. W. Schmidt, Dr. I. Sergueev, Dr. M. B. Stone, Dr. J. Voigt, Dr. H.-C. Wille, Prof. Th. Brückel, Prof. F. Grandjean, Prof. D. C. Johnson, Prof. S. M. Kauzlarich, Prof. V. Keppens, Prof. Gary J. Long, Prof. A. Schengelaya and Prof. H. Schober for their help during experiments, for corrections and advises as well as for helpful discussions.

I would like to thank all my colleagues from the Institute of Scattering Methods and particularly Mr. B. Schmitz for his technical assistance.

For the funding of my PhD thesis I would like to acknowledge the Forschungszentrum Jülich GmbH and the Helmholtz Association of German Research Centres, through to funding of the "Lattice Dynamics in Emerging Functional Materials" Investigator Group. I thank Prof. Th. Brückel for financial support at the beginning of my thesis.

The European Synchrotron Radiation Facility, the Advanced Photon Source, the Spallation Neutron Source, the Paul Scherrer Institut, the Institut Laue-Langevin, the Forschungs-Neutronenquelle Heinz Maier-Leibnitz (FRM II) and the Jülich Centre for Neutron Science are acknowledged for provision of synchrotron and neutron beam time.

I want to particularly thank my parents for their support and confidence.

Finally, I want to thank my boyfriend Andreas for his support, his technical assistance, his patience and his love.

Publication Dissertation

Chapter 2−5 of this dissertation are manuscripts that are submitted or will be submitted shortly and formatted in RevTex4.

Chapter 2:

A. Möchel, I. Sergueev, N. Nguyen, Gary J. Long, F. Grandjean, D. C. Johnson, and R. P. Hermann, **Lattice Dynamics in the $FeSb_3$ Skutterudite**, submitted to *Phys. Rev. B*, March 2011.

Chapter 3:

A. Möchel, I. Sergueev, H.-C. Wille, J. Voigt, M. Prager, M. B. Stone, B. C. Sales, Z. Guguchia, A. Shengelaya, V. Keppens, and R. P. Hermann, **Lattice dynamics and anomalous softening in the $YbFe_4Sb_{12}$ skutterudite**, to be submitted to *Phys. Rev. B*, May 2011.

Chapter 4:

A. Möchel, W. Schweika, K. Schmalzl, B. C. Sales, and R. P. Hermann, **Experimental study of the phonon dispersion in the $Sr_8Ga_{16}Ge_{30}$ clathrate**, to be submitted to *New Journ. Phys.*, June 2011.

Chapter 5:

A. Möchel, I. Sergueev, H.-C. Wille, F. Juranyi, H. Schober, W. Schweika, S. R. Brown, S. M. Kauzlarich, and R. P. Hermann, **Lattice dynamics in the thermoelectric Zintl compound $Yb_{14}MnSb_{11}$**, to be submitted to *Phys. Rev. B*, May 2011.

Abstract

A brief introduction to the thermoelectric effects, the studied materials, and the experimental methods is given in the first chapter. The introduction is not intended to be exhaustive, but only to summarize important basic information for the reader. The introduction is followed by four chapters dedicated to detailed experimental studies of the lattice dynamics in selected thermoelectric Zintl phases.

First, the lattice dynamics in the unfilled and filled skutterudites $FeSb_3$, $CoSb_3$, and $YbFe_4Sb_{12}$ were studied by nuclear inelastic scattering, inelastic neutron scattering, and several macroscopic methods. These studies reveal that $FeSb_3$ exhibits softer Sb bonds than $CoSb_3$, that the density of phonon states is shifted towards lower energies and the velocity of sound is lower in $FeSb_3$ as compared to $CoSb_3$. It appears thus that the soft $[Fe_4Sb_{12}]$ framework dynamics might play an important role in the thermoelectric properties of filled skutterudites. The observed anomalous temperature dependence of the elastic constants and the rearrangement of the spectral weight of the Yb phonon states in $YbFe_4Sb_{12}$ can be explained by a change of the Yb valence state with the temperature.

Second, the lattice dynamics in the $Sr_8Ga_{16}Ge_{30}$ clathrate was investigated by inelastic neutron scattering measurements on a single crystal. We found that several mechanisms contribute to the low thermal conductivity in this system and that the reduction of the heat capacity contribution to the thermal conductivity plays a significant role to the low thermal conductivity, besides the reduction in the phonon lifetime and the phonon group velocity that is related to the guest atom.

Third, the lattice dynamics of the Zintl phase $Yb_{14}MnSb_{11}$ was studied by inelastic neutron scattering and nuclear inelastic scattering measurements. All phonon modes of these complex crystal systems are in a narrow energy range below $\sim$25 meV and the Debye temperature, the velocity of sound and the mean force constants are small compared to those of other thermoelectric materials such as Zn_4Sb_3. By comparing the lattice dynamics in $Yb_{14}MnSb_{11}$ and Zn_4Sb_3 different mechanisms which lead to the low thermal conductivity in Zintl phases have been identified. Between 300 and 1200 K no softening of the velocity of sound in $Yb_{14}MnSb_{11}$ was observed by temperature dependent inelastic neutron scattering measurements, which is in line with its large melting temperature.

Résumé

Le premier chapitre introduit brièvement les effets thermoélectriques, les matériaux étudiés et les techniques expérimentales utilisées. Cette introduction ne se veut pas exhaustive, mais résume seulement les informations essentielles pour le lecteur. Cette introduction est suivie de quatre chapitres dédiés aux études expérimentales détaillées des la dynamique de réseau dans une sélection de phases de Zintl thermoélectriques.

Premièrement, la dynamique de réseau dans les skuttérudites vides et remplies $FeSb_3$, $CoSb_3$, et $YbFe_4Sb_{12}$ ont été étudiées par diffusion nucléaire résonante inélastique, diffusion inélastique de neutrons ainsi que diverses techniques macroscopiques. Ces études révèlent que $FeSb_3$ possèdent des liaisons de Sb plus faibles que dans $CoSb_3$ et que par ce fait, la densité d'états de phonons est déplacées vers des énergies plus faibles et que la vitesse du son dans $FeSb_3$ est réduite par rapport à $CoSb_3$. Il apparaît donc que la dynamique de l'ossature structurelle [Fe_4Sb_{12}] puisse jouer un rôle important dans les skuttérudites remplies. La dépendance en température anomale des constantes élastiques et le réarrangement du poids spectral des états de phonons de Yb dans $YbFe_4Sb_{12}$ a été étudié et peut s'expliquer par une modification de l'état de valence de Yb en fonction de la température.

Deuxièmement, la dynamique de réseau dans la clathrate $Sr_8Ga_{16}Ge_{30}$ a été étudiée par diffusion inélastique de neutrons sur un monocristal. Nous avons mis en évidence que plusieurs mécanismes contribuent à la faible conductivité technique dans ce système et que la réduction de la chaleur spécifique partielle contribuant à la conductivité thermique joue un rôle significatif pour la faible conductivité thermique, à côté de la réduction tant du temps de vie des phonons que de leur vitesse de groupe, une réduction liée aux atomes hôtes.

Troisièmement, la dynamique de réseau de la phase de Zintl $Yb_{14}MnSb_{11}$ a été étudiée par diffusion inélastique de neutrons et diffusion nucléaire inélastique. Tous les modes de phonons de cette structure cristalline complexe se trouvent dans un bande d'énergie étroite en deçà de $\sim$25 meV et que la température de Debye, la vitesse du son et les constantes de forces moyennes sont faibles par rapport à d'autres matériaux thermoélectriques, tels que Zn_4Sb_3. Par comparaison, les mécanismes différents qui contribuent à la faible conductivité dans les phases de Zintl $Yb_{14}MnSb_{11}$ et Zn_4Sb_3 ont été étudiés. Aucune réduction significative de la vitesse du son dans $Yb_{14}MnSb_{11}$ entre 300 et 1200 K n'a été observée par diffusion inélastique de neutrons, ce qui est en accord avec la température de fusion élevé de ce matériau.

Kurzbeschreibung

Im ersten Kapitel ist eine kurze Einleitung zu den thermoelektrischen Effekten, den untersuchten Materialien und den experimentellen Methoden gegeben. Diese Einleitung erhebt keinen Anspruch auf Vollständigkeit und sie ist als eine kurze Einführung in die Grundlagen für den Leser gedacht. Der Einleitung folgen vier Kapitel welche den detailierten experimentellen Studien zu der Gitterdynamik in thermoelektrischen Zintl Phasen gewidmet sind.

Erstens: Die Gitterdynamik wurde in den ungefüllten und gefüllten Skutteruditen $FeSb_3$, $CoSb_3$ und $YbFe_4Sb_{12}$ mit Hilfe der inelastischen Kernresonanz, der inelastischen Neutronenstreuung und unterschiedlichen makroskopischen Messmethoden untersucht. Diese Untersuchungen zeigen, dass $FeSb_3$ weichere Sb Bindungen aufweist als $CoSb_3$, die Phononenzustandsdichte zu tieferen Energien hin verschoben ist und die Schallgeschwindigkeit in $FeSb_3$ niedriger als in $CoSb_3$ ist. Daher scheint die Dynamik der $[Fe_4Sb_{12}]$ Grundstruktur eine wichtige Rolle für die thermoelektrischen Eigenschaften in gefüllten Skutteruditen zu spielen. Der anomale Temperaturverlauf der elastischen Konstanten und die Umordnung der Yb Phononenzustände in der Phononenzustandsdichte von $YbFe_4Sb_{12}$ wurden untersucht und können durch die temperaturabhängige Änderung des Yb Valenzzustandes erklärt werden.

Zweitens: Die Gitterdynamik des $Sr_8Ga_{16}Ge_{30}$ Clathrates wurde durch inelastische Neutronenstreumessungen an einem Einkristall untersucht. Es wurde herausgefunden, dass verschiedene Mechanismen für die niedrige thermische Leitfähigkeit dieses Systemes verantwortlich sind und dass die Reduzierung des Wärmekapazitätsbeitrages zu der thermischen Leitfähigkeit, neben der Reduzierung der Phononenlebenszeit und der Phononengruppengeschwindigkeit durch das Gastatom, ein weiterer wichtiger Faktor für die niedrige thermische Leitfähigkeit ist.

Drittens: Die Gitterdynamik der Zintl Phase $Yb_{14}MnSb_{11}$ wurde durch inelastische Neutronenstreuung und inelastische Kernresonanzmessungen untersucht. Alle Phononenmoden dieses komplexen Kristallsystems liegen in einem Energiebereich unterhalb von $\sim$25 meV und die Debyetemperatur, die Schallgeschwindigkeit und die mittleren Kraftkonstanten sind niedrig im Vergleich zu anderen thermoelektrischen Materialien wie Zn_4Sb_3. Durch den Vergleich der Gitterdynamik in $Yb_{14}MnSb_{11}$ zu der in Zn_4Sb_3 wurden die unterschiedlichen Mechanismen, welche zu den niedrigen thermischen Leitfähigkeiten in Zintl Phasen führen, bestimmt. In den temperaturabhängigen inelastischen Neutronenstreumessungen wurde für $Yb_{14}MnSb_{11}$ keine Erniedrigung der Schallgeschwindigkeit zwischen 300 und 1200 K festgestellt, was in guter Übereinstimmung mit der hohen Schmelztemperatur ist.

Contents

Chapter 1

General Introduction

This introduction is not intended to be exhaustive, but only to summarize important basic information for the reader. General references for the sections are indicated next to the section title.

I. THERMOELECTRICITY[1–4]

The environmentally friendly generation and conversion of energy is an important task due to our increasing power consumption and its large influence on the climate related to conventional methods of fossil energy conversion. Thermoelectric materials can be used to convert heat into electricity by harnessing the Seebeck effect. Conversely, cooling can be achieved via the Peltier effect. The functionality of a thermoelectric couple, which is used in thermoelectric devices, is illustrated in Fig. 1: Thermoelectric couples consist of two semiconducting legs, namely one that transports negative charges (n-type) and the other one that transports positive charges (p-type). The semiconducting legs possess a difference in the Fermi energy. Thus, the charge carriers have different transport energies in the different legs. If a current passes from one leg to the other, the transported energy of the carriers is modified and the difference appears as heating or cooling in the junction. Conversely, if the junction is heated, the carriers can pass from one material with lower carrier energy to the other material with higher carrier energy. This yields an electromotive force and in a closed circuit a current flows. A good thermoelectric material has to possess a good electrical conductivity and a small thermal conductivity, because its efficiency is proportional to the figure of merit, $ZT = \sigma\alpha^2 T/\kappa$, with the electrical conductivity, σ, the material dependent Seebeck coefficient, α, and the thermal conductivity κ. Thus, a good thermoelectric material should both behave as an electron crystal and a phonon glass[5]. Nowadays, Peltier elements are mainly used in applications, where noiseless, cryogen gas free or space saving cooling devices or bipolar cooling are requested, *e.g.* in minibar fridges or sample array coolers in biology. For energy conversion, thermoelectric devices are used, if a compact and maintenance free device is needed, *e.g.* in spacecrafts. The potential use as converter of waste heat, *e.g.* for recovering energy from the exhaust gas of an automobile, into electricity has only prototype value today, due to the low efficiency of the state of the art thermoelectric devices. One way to increase the ZT and therefore the efficiency, is to reduce the thermal conductivity without changing the electrical properties. In a semiconductor, heat is transported by electrical car-

riers and phonons, *i.e.* the thermal conductivity has an electrical and a lattice contribution. PbTe and SiGe, which are common thermoelectric materials used today, exhibit thermal conductivities of ∼2.2 W/(m K) at 300 K and ∼3.5 W/(m K) at 900 K, respectively[6,7] and possess a ZT value of ∼0.8 and ∼0.4, respectively, at the indicated temperatures[7]. In order to achieve a high ZT value, the lattice part of the thermal conductivity has to be reduced. Because the electrical part is strongly dependent on the electrical resistivity, a lowering of the electrical thermal conductivity would also lead to a lowering of the electrical resistivity and the ZT value would not be enhanced. In the simple kinetic gas theory, the lattice thermal conductivity is dependent on the specific heat capacity, C_V, the mean velocity of sound, v_s, and the mean free path of the phonons, λ: $\kappa_L = C_V v_s \lambda/3$. One approach of lowering the lattice thermal conductivity in bulk materials is the filling of cage structures, *e.g.* skutterudites or clathrates, with heavy atoms, such as Yb, Sb or Eu. The dynamics of the filler impedes the thermal transport by reducing the mean free path of the phonons as well as the mean phonon velocity, and both effects contribute to a lower thermal conductivity. Another approach is the use of complex crystal systems with a large number of atoms in the unit cell, *e.g.* $Yb_{14}MnSb_{11}$, where the contribution of the heat capacity to the thermal conductivity is reduced. Nanostructuring, nanoinclusions and lowering the dimensionality are other approaches to reduce the thermal conductivity by phonon confinement.
This work is focused on a detailed experimental study of the lattice dynamics in thermoelectric bulk Zintl phases, in order to investigate the mechanisms that lead to the low thermal conductivity as observed in these systems.

II. ZINTL FORMALISM[8]

Zintl phases are intermetallic compounds of electropositive metals, such as alkaline, alkaline earth and lanthanides, and metals with a medium electronegativity. The cations are electron donors to the anionic sublattice. The typically larger anions form the structure and generates subunits, *i.e.* polyanions, similar to the isoelectronical pure elements, *e.g.* in the compound NaTl the $[Tl^-]$ anions are forming a diamond structure in which the Na^+ ions are located. Zintl phases most often obey the general valence rule. The rich chemistry of Zintl phases offers numerous possibilities for chemical substitutions and structural modifications that allows the tuning of the fundamental transport parameters in order to improve

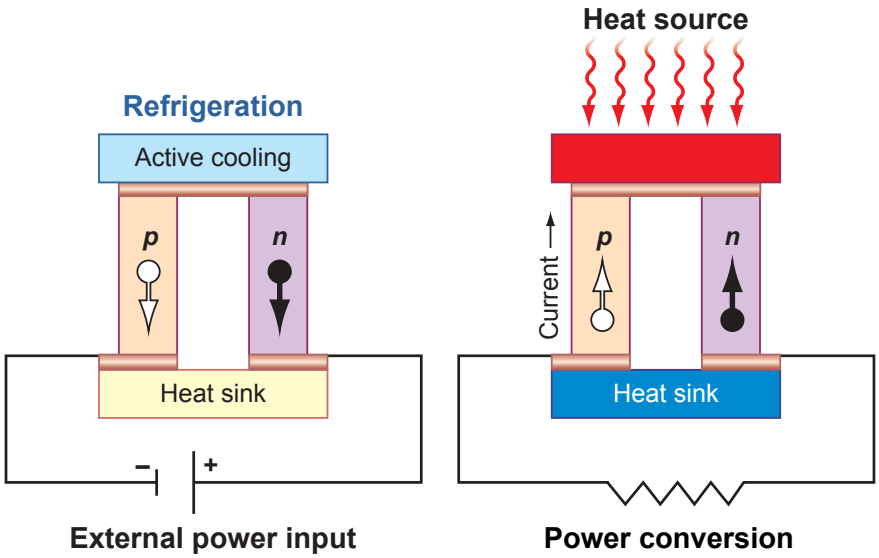

FIG. 1. Illustration of the Peltier, left, and Seebeck effect, right, in a thermoelectric couple [2].

the thermoelectric performance[9]. Herein, the following compounds, which obey the Zintl formalism, are studied:

a) Skutterudites: In the unfilled skutterudite $FeSb_3$ the unit cell contains 8 formula units and consist of a network of corner sharing $[FeSb_6]$ octahedrals. Fe has a formal valence state of 3+ whereas Sb has a formal valence state[10] of 1−. By filling the structure with Yb, which has a valence state of 2+ at 300 K, the average Fe valence state is lowered to 2.5+ in the $YbFe_4Sb_{12}$ compound. The valence state of the Sb anionic sublattice does not change. b) Clathrates: In $Sr_8Ga_{16}Ge_{30}$ the unordered polyanions consisting of Ga^{1-} and Ge^0 form two types of cages[1], namely a dodecahedron of 20 Ga and Ge atoms and a tetrakaidecahedron of 24 Ga and Ge atoms. The Sr^{2+} is located in both cage types. c) $Yb_{14}MnSb_{11}$: The structure is generated by 8 units of a $MnSb_4^{9-}$ tetrahedron, a Sb_3^{7-} polyanion and 4 Sb^{3-} anions, whereas the Yb^{2+} are donating 28 electrons[11].

III. STUDIED MATERIALS

A. Skutterudites

Skutterudites, see Fig. 2, have[1] cubic crystal structure with the space group $Im\bar{3}$. The archetype material is the mineral $(Co,Ni)As_3$. Skutterudites are promising thermoelectric materials due to the possibility of tuning the thermal properties by filling the cage structure

with only slight changes of the electronic properties[12] and the typical thermal stability up to ∼800 K. It was suggested[13,14] that by filling the skutterudite framework, [Co_4Sb_{12}] or [Fe_4Sb_{12}], with lanthanides, such as La, Eu of Yb, which have large masses in comparison to the host atoms, the thermal conductivity will be reduced. This reduction of the thermal conductivity, κ, by filling the structure with heavy elements was verified[14,15] in several compounds, *e.g.* in $La_{0.3}Co_4Sb_{12}$ and $CeFe_{0.75}Co_{3.25}Sb_{12}$, which shows a reduction of the thermal conductivity by 78% and 85%, respectively, compared to the unfilled compound $CoSb_3$. The precise mechanism behind the reduction in κ caused by the filler in skutterudites and clathrates, see below, is still an open question. One suggestion for the reduction mechanism of the thermal conductivity was that the 'rattling' of the filler compound has an influence on the lattice dynamics of the host structure[16]: The phonon mean free path is reduced by the movement of the filler and therefore the thermal conductivity is reduced. Another suggestion for the reduction of the thermal conductivity is that through the interaction of the guest and the host modes the acoustic phonon modes are flattened and due to this avoided crossing the velocity of sound is reduced[17]. It was also suggested that the interaction of the low energy optical guest modes and the acoustic phonon modes lead to Umklapp scattering, which hinders the heat transport[18], but that otherwise skutterudites behave as a conventional phonon crystal and not as a phonon glass. Another approach to increase the ZT value is the enhancement of the electrical properties by doping[12]. This will not be regarded in this work.

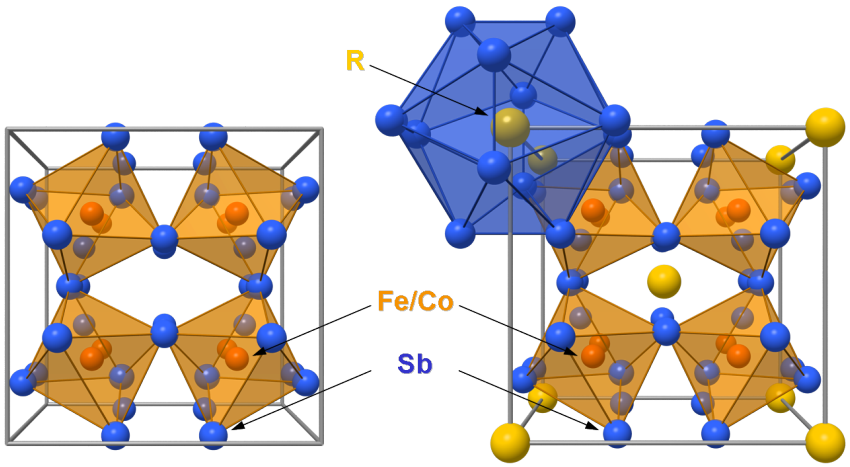

FIG. 2. The unfilled (left) and filled (right) skutterudite structure. Blue, red and yellow indicates Sb, Fe or Co and the filler R, respectively.

In this work the lattice dynamics in the filled and unfilled skutterudites, $YbFe_4Sb_{12}$ and $FeSb_3$, respectively, were studied. Due to the poor electrical properties, $YbFe_4Sb_{12}$ exhibits[19] a low ZT value of ∼0.02 at 300 K. Nevertheless, because of the low thermal conductivity of 2 W/(m K) at 300 K[19] it is a useful model system for investigating the influence of the filler on the thermal conductivity. In the temperature dependence of the elastic constants of $YbFe_4Sb_{12}$, an anomaly was found at ∼50 K and the reason of this anomaly is likely a change of the Yb valence state with temperature, see Chapter 3. The unfilled parent compound $FeSb_3$ is metastable[20] and can be prepared only as films, see Chapter 2. The synthesis of a pure phase film was recently successful and the structure, the electrical conductivity, the magnetism and the lattice dynamics were studied. This study reveals that $FeSb_3$ is softer in the lattice dynamics than the isostructural compound $CoSb_3$, see Chapter 2. The characterization of the Seebeck coefficient and the thermal conductivity could not carried out so far, therefore a ZT value is not available.

B. Clathrates

Clathrates are host-guest complexes[1,8] and the two archetypes have the general formula $X_2Y_6E_{46}$ (type I), *e.g.* $Sr_8Ga_{16}Ge_{30}$, and $X_8Y_{16}E_{136}$ (type II), *e.g.* Na_3Si_{136} [21], where X and Y are the guest atoms, while the E atoms are forming the host structure. In this work, the lattice dynamics in the type I clathrate $Sr_8Ga_{16}Ge_{30}$ were studied. The same mechanisms behind the low thermal conductivity in clathrates were suggested as for skutterudites, see above. The comparison with an unfilled system is not possible in this case, because the unfilled Ga-Ge clathrate is structurally unstable without the filler atom[22], however recently empty Si and Ge chlatrates have been synthesized[23] and further studies on their lattice dynamics will certainly be of high interest. $Sr_8Ga_{16}Ge_{30}$ crystallizes in the cubic space group $Pm\bar{3}n$, see Fig. 3. Other isostructural systems exist such as $Ba_8Ga_{16}Ge_{30}$ and Na_8Si_{46}, which are also candidates for thermoelectric applications. Sr can occupy the center of two different cages, the smaller dodecahedron of 20 Ga and Ge atoms and the larger tetrakaidecahedron of 24 Ga and Ge atoms. It was found[24] that the Sr atoms sitting in the larger cage play the predominant role in the reduction of the thermal conductivity. $Sr_8Ga_{16}Ge_{30}$ exhibits[25] a thermal conductivity of 1 W/(m K) at 300 K. With the electrical resistivity and the Seebeck coefficient[26] of $\rho = 2$ mΩ cm and $S = -115$ μV/K, respectively, at room temperature, a

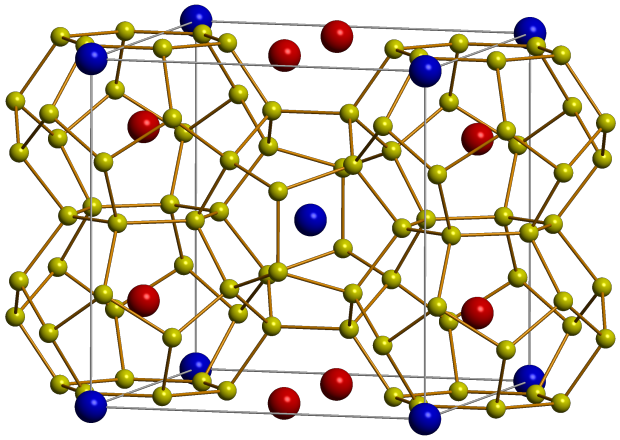

FIG. 3. The crystal structure of the $Sr_8Ga_{16}Ge_{30}$ clathrate. Yellow indicates Ga and Ge and blue and red the Sr atom sitting in the smaller and larger cage, respectively.

modest ZT of 0.02 was obtained for $Sr_8Ga_{16}Ge_{30}$. In order to investigate the lattice dynamics in $Sr_8Ga_{16}Ge_{30}$, the phonon dispersion was studied by inelastic neutron scattering measurements on a single crystal and the findings are summarized in Chapter 4. It was found that beside the reduction of the phonon lifetime and the phonon velocity by the influence of the guest atom the lowering of the heat capacity of the acoustic phonons and thus the heat capacity contribution to the thermal conductivity is also an important mechanism, which yields to the low thermal conductivity in $Sr_8Ga_{16}Ge_{30}$.

C. $Yb_{14}MnSb_{11}$

The Zintl phase $Yb_{14}MnSb_{11}$ crystallizes[11] in the tetragonal space group $I4_1/\,a\;c\;d$. The large unit cell of ∼6060 Å consists of 208 atoms, see Fig. 4. This material exhibits[27] a nearly temperature independent low thermal conductivity of 0.8 W/(m K) between 300 and 1200 K, which is in the range of the thermal transport coefficient of glasses. Combined with the good electrical properties above 900 K a ZT value of 0.8 at 1000 K is observed. Furthermore, the material stays solid up to ∼1300 K, which makes this system a promising candidate for thermoelectric applications in the high temperature range, *e.g.* for radioisotope thermoelectric generators as used in spacecrafts. It was suggested[9] that one reasons for the low thermal conductivity is the small contribution of the heat capacity to the thermal conductivity, due

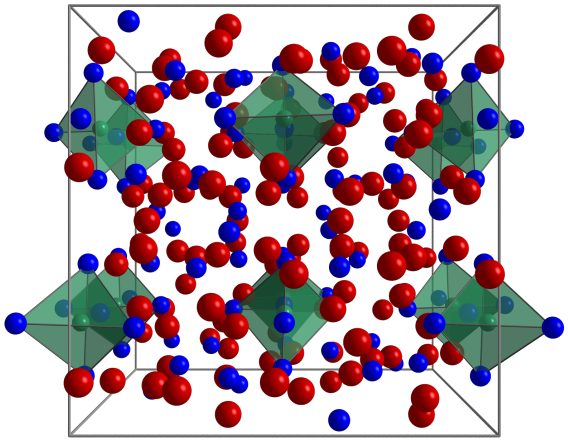

FIG. 4. Crystal structure of $Yb_{14}MnSb_{11}$. The red, blue and green spheres represent the Yb, Sb and Mn atoms, respectively.

to the large unit cell volume. The heat capacity is equally divided to all phonon modes and because of the small optical phonon velocity, the heat transport is mainly through the acoustic phonons. Due to the small ratio of acoustic to optical modes in $Yb_{14}MnSb_{11}$ compared to systems with a smaller number of atoms in the unit cell, the contribution of the heat capacity to the thermal conductivity is low. Furthermore, it was empirical derived[9,28] that in structures, which exhibit a large difference in the atom masses, such as $Yb_{14}MnSb_{11}$, the heat transport through the optical modes can be neglected. The lattice dynamics were studied in this system and the results are summarized in Chapter 5. It was found that another important mechanism which lead to the low thermal conductivity in this system, is the low velocity of sound, beside the reduction of the heat capacity contribution to the thermal conductivity.

IV. MACROSCOPIC MEASUREMENTS

A. Heat Capacity Measurements[3]

Specific heat capacity measurements at constant pressure, C_P, were done using a physical properties measurement system from Quantum Design (QD-PPMS) with a commercially available setup[29]. The sample holding puck is shown in Fig. 5. The platform is connected

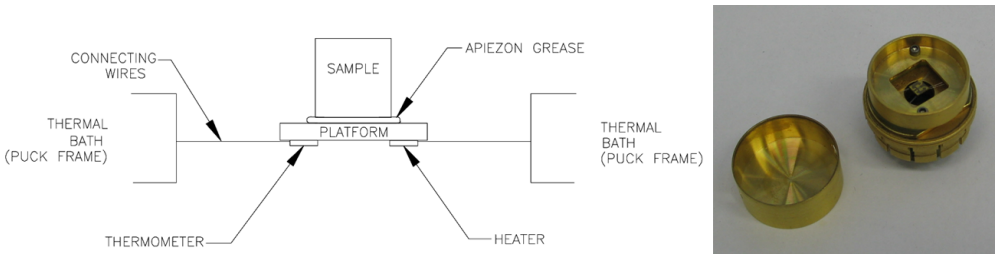

FIG. 5. The setup of the puck for measuring the heat capacity, from Ref. [29], and a photo of the puck.

to the frame of the puck by 8 wires. A small amount of grease between sample and the platform guarantees the thermal contact. During the measurements, the puck is in high-vacuum of $\sim 10^{-5}$ mbar. Therefore, the only thermal connection to the platform are the wires. To measure the heat capacity, a heat pulse is applied to the platform, (heater in Fig. 5) and therefore to the sample and the heat relaxation time of the platform with the sample is measured (thermometer in Fig. 5). From the relaxation time of the platform with the sample, the heat capacity C_P can be calculated in first approximation by $\tau = C_P/K_W$, with the inverse relaxation time τ and the thermal conductivity of the wires K_W. In a more complete model, the non ideal coupling of the sample to the platform is considered and the heat capacity was corrected for this.

The dominant contributions to the heat capacity of non-magnetic materials is the electronic and the lattice vibration contribution. At low temperatures, the electronic contribution shows a linear dependence with the temperature, whereas the lattice contribution has a cubic dependence with the temperature. At elevated temperatures, the lattice contribution is the dominant part in the heat capacity. Lattice dynamical properties can be obtained from the heat capacity. There are two models for the lattice vibrations: In the Debye model it is assumed that all atoms move collectively and that the dependence of the frequency to the wavevector, $\vec{k}$, of the collective motion, *i.e.* the phonons, is linear up to the Debye frequency. This approximation describes more or less accurately the acoustic phonons, see below. The Debye frequency, ω_D, is proportional to the Debye temperature $\theta_D = \hbar\omega_D/\mathrm{k_B}$. The underlying assumption of the Einstein model is that all atoms vibrate independently from each other with the same frequency, the Einstein frequency. This model is an idealization of optical phonons. The Einstein temperature θ_E is proportional to the Einstein frequency, ω_E. The lattice part of the heat capacity has contributions both from

the optical and the acoustic phonons and a combination of the Debye and Einstein models can be used for the heat capacity. In the Debye model, the specific heat can be expressed by: $C_V = 9nk_B(T/\theta_D)^3 \int_0^{\theta_D/T} x^4 \exp(x)dx/(\exp(x)-1)^2$, with $x = (\hbar c\vec{k})/(k_B T)$, the speed of light, c, and the wavevector $\vec{k}$. In the Einstein model, the specific heat is expressed by: $C_V = pnk_B(\theta_E T)^2 \exp(\theta_E T)/(\exp(\theta_E T)-1)^2$, with the number of primitive cells per unit volume n and the number of optical branches p. From the temperature dependence of the heat capacity, the Debye and Einstein temperatures can be obtained. These models are only approximations but nevertheless the models are useful in order to compare different materials and these models give an insight into the lattice dynamics.

B. Magnetization and Resistivity Measurements[29]

In order to precharacterize the samples, magnetization and resistivity measurements are useful, because the magnetism and the resistivity of a sample is strongly dependent on the phase, the microstructure and on impurities in the sample. Magnetization measurements were carried out on a QD-PPMS using the vibrating sample magnetometer, VSM, option. The VSM is a DC magnetometer with a sensitivity of $\sim 10^{-5}$ emu and a magnetic field up to 9 T can be applied to the sample. The setup is shown in Fig. 6. The sample vibrates between the pickup coils with a frequency of 40 Hz, inducing a voltage in the coils. The induced voltage is proportional to the magnetic moment of the sample. By changing the temperature or the applied magnetic field, the susceptibility or the hysteresis of the sample can be measured. The obtained results have to be corrected for the diamagnetic contribution of the sample holder, see also Chapter 2.

The electrical resistivity was measured with a commercially available option for a QD-PPMS using the four point method. A sketch of the sample holder setup, with which 3 samples can be measured at the same time, is shown in Fig. 6. The four wires are connected to each sample by silver paint and to the sample holder by soldering the wires to the voltage and current contacts. Thin silver wires were used for the measurements in this work. A DC current is applied to the sample (I+ and I−) and the resulting voltage is measured between the V+ and V− contacts. The distance between the voltage contacts on the sample, l, and the cross section of the sample, A, has to be known, in order to calculated the specific electrical resistivity by $\rho = VA/(Il)$.

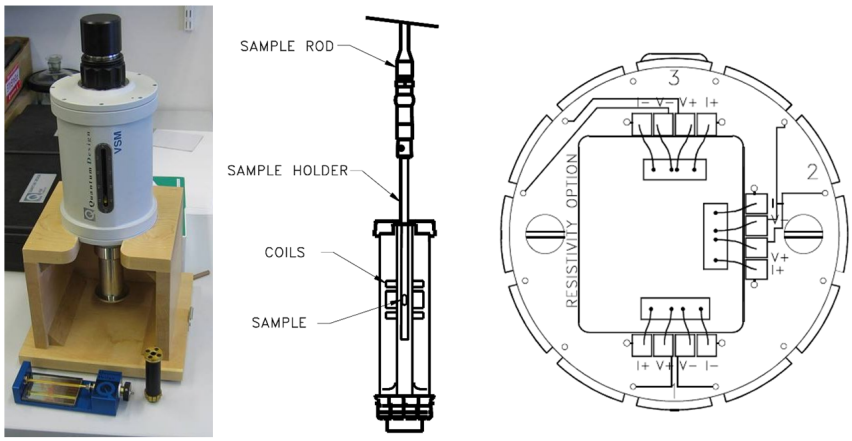

FIG. 6. The VSM setup and a photo of the motor, the sample holder and the coil puck (left) and the setup for resistivity measurements (right), from Ref. [29].

C. Resonant Ultrasound Spectroscopy

With the resonant ultrasound spectroscopy the elastic constants and therefore the velocity of sound can be measured[30]. The sample is clamped between two piezoelectric transducers, such that it has no other contact apart from the transducers, see Fig. 7. One transducer emits ultrasound waves with frequencies in the MHz range. The other transducer acts as a receiver. If the incoming wave has a frequency which is a full body resonance of the sample, a strong response signal is recorded. In the approximation of a homogeneous sample the resonant frequencies of the sample depend on the elastic constants, the density, and the geometry of the sample. By tuning the incoming frequency, various resonant frequencies can be determined and with the knowledge of the density and the geometry of the sample, the elastic constants can be obtained by a fit of the frequency spectrum. Different finite element models for different sample geometries, *e.g.* for parallelepiped-shaped, spherical and cylindrical samples exist. In order to minimize the error bars of the obtained elastic constants, the shape of the sample has to be as close as possible to the sample geometry used for the model, with a typical tolerance of less than 2% in any linear dimension or angle.

From a measurement of a polycrystalline sample two independent elastic constants can be obtained, c_{11} and c_{44}. The shear modulus,c_{44}, is typically denoted as G. From c_{11} and c_{44} the Young modulus, $E = (3c_{44}c_{11} - 4c_{44}^2)/(c_{11} - c_{44})$, the Poisson ratio, $\nu = (E/(2G)) - 1$, and

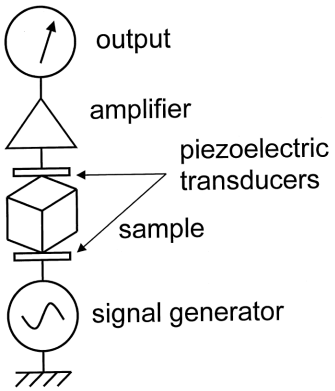

FIG. 7. The setup for the resonant ultrasound spectroscopy [34].

the bulk modulus, $B = E/(3(1-2\nu))$, can be obtained[31]. Furthermore, the isotropic average of the longitudinal and the transversal velocity of sound can be obtained by $v_L^2 = c_{11}/\rho$ and $v_T^2 = c_{44}/\rho$, respectively, with ρ as the density of the material. The mean velocity of sound can be calculated by $v_s = (1/3 * (2/v_T^2 + 1/v_L^2))^{-1/3}$. The velocity of sound is proportional to the thermal conductivity and an important parameter for the lattice dynamics, see Chapter 4. From single crystal sample measurements, all independent elastic constants can be obtained.

By the temperature dependence of the elastic constants, magnetic or structural phase transitions and anomalies can be studied. The typical temperature dependence of the elastic constants can be described by a phenomenological Varshni model[32]. If an anomaly or a phase transition occurs, a dip or a kink will be observed in the temperature dependence. The temperature dependence of the elastic constants was studied[33] in filled skutterudites and a deviation from the Varshni function was seen as a dip at 50 K. The reason for this anomaly is the dynamics of the filler atom, which can be described as an Einstein oscillator. By taking the response of such a Einstein oscillator into account, the anomalous temperature dependence can be modeled[33]. This localized phonon mode was also observed in the density of phonon states measured by inelastic neutron scattering. Herein, the study of the elastic constants and the density of phonon states of $YbFe_4Sb_{12}$ will be reported in Chapter 3.

V. ELASTIC SCATTERING AND DIFFRACTION[3,35]

In a scattering process, the scattering particle, *e.g.* neutrons, electrons or photons, are described by waves with the wavevector $\vec{k} = 2\pi/\lambda$. The wavelength, λ, is equivalent to

the energy, E, and the mass, m, of the particle by the de Broglie relation $\lambda = h/(mv) = h/(\sqrt{2mE})$, with the velocity v. For photons, where $v = c$, $\lambda = hc/E$. The scattering vector, $\vec{Q}$, is defined by the difference between the incident and the final wavevector, $\vec{k}_i$ and $\vec{k}_f$, respectively, by $\vec{Q} = \vec{k}_f - \vec{k}_i$. In an elastic process, the absolute value of the wavevector is not changed, $|\vec{k_i}| = |\vec{k_f}|$. Scattering takes place, if the scattering vector is equal to an reciprocal lattice vector $\vec{G}$, $|\vec{Q}| = |\vec{G}| = 2\sin\theta|\vec{k_f}| = 4\pi\sin\theta/\lambda$. θ is the angle between the incident beam and the scattering plane and in an elastic scattering process the angle between the scattered beam and the scattering plane is equal to θ. With the distance between the scattering planes, d, and $|\vec{Q}| = 2\pi/d$, Bragg's law is obtained: $n\lambda = 2d\sin\theta$. In other words, constructive interference takes place, if the angle θ is chosen, so that the path difference between neighboring waves, which is related to d, is an integer multiple n of the incident wavelength, which means that the scattered waves are in phase and a diffraction maximum can be detected. From several d values of different directions as given by the Miller indices h, k and l, the lattice parameters can be determined. For rectangular lattice systems, *i.e.* cubic, orthorhombic and tetragonal crystal systems, the formula $d = 1/(\sqrt{(h^2/a^2 + k^2/b^2 + l^2/c^2)})$ yields the lattice parameter a, b and c.

In a diffraction measurement, a broad θ range will be studied without an energy resolution. Reflections, which obey Bragg's law for several h, k and l combinations, defined by the space group of the material, arises at defined angles. From the positions of the reflections the lattice parameter can be obtained. The intensity, I, of the reflections are proportional to the differential cross section, $I \sim (d\sigma/d\Omega)$, with the cross section σ and the distribution angle Ω. Since the scattering does not take place on a point, but on an object with finite dimension, a form factor, $f(\vec{Q})$, has to be implied: $(d\sigma/d\Omega)_{total} = (d\sigma/d\Omega)_{point} \cdot |f(\vec{Q})|^2$. For x-ray's, which are scattered by the electron cloud of the atoms, the atomic form factor is defined as the Fourier transformation of the charge distribution $f(\vec{Q}) = \int \rho(\vec{r}) \exp(i\vec{Q}\vec{r}) d^3r$, with the electron density ρ and the equilibrium position of the atoms $\vec{r}$. If there are different atoms in the unit cell, the structure factor is obtained by summing over the form factors of each atom in the unit cell with appropriate phase shift. Due to thermal motions, the atoms are vibrating around their positions $\vec{r}$. If an atom is not on the equilibrium position, the condition for constructive interference is not fulfilled. Therefore, the intensity of these reflections can be lowered depending on the size of the thermal excitation, which is temperature dependent. This is taken into account by the Debye-Waller factor $f'(\vec{Q}) = f(\vec{Q}) \cdot \exp(-2\pi^2 u^2/d^2)$,

with the mean-square displacement u^2. Therefore, from the position and intensity of the reflections, the positions of the atoms in the unit cell, the occupation of the atom sites and the mean square displacements can be obtained. In this work, x-ray diffraction measurements were performed at a Huber G670 diffractometer with copper $K_{\alpha 1}$ radiation in a Guinier geometry using an imaging plate detector and at the Advanced Photon Source, APS, with synchrotron radiation in Debye-Scherrer geometry using an imaging plate detector. The diffraction patterns were refined by the Rietveld method using the FULLPROF[36] program.

The Grüneisen coefficient describes the dependence of the phonon mode frequency, $\omega(\vec{k})$, to the volume of a unit cell, V: $\gamma = -\partial(\ln\omega(\vec{k}))/(\partial(\ln V))$ and indicates the deviation of the lattice dynamics from the harmonic approximation, see below. The thermal conductivity is related to the anharmonicity and therefore the Grüneisen parameter is a useful parameter in order to compare thermoelectric materials. From the temperature dependence of the lattice parameters, $a(T)$, the thermal expansion coefficient, α, can be obtained by the derivative $\alpha = (da(T)/dT)/a(300K)$. The Grüneisen coefficient follows from the thermal expansion, the bulk modulus B, obtained *e.g.* by resonant ultrasound spectroscopy, the heat capacity C_V and the molar volume V_m: $\gamma = 3\alpha B V_m/C_V$, see Chapter 2, 3 and 5.

VI. INELASTIC SCATTERING[3,35,37]

Inelastic scattering takes place, if there is an energy transfer between the scattered radiation and the probed object. Due to the energy transfer a creation or an annihilation of lattice vibrations, *i.e.* phonons, takes place. Inelastic scattering is thus a suitable method to study the lattice dynamics in materials. In this work, inelastic neutron scattering and nuclear inelastic scattering were used in order to investigate the lattice dynamics, and therefore to study the related thermal conductivity in thermoelectric Zintl phases.

Phonons are quantized collective vibrations of atoms around their equilibrium positions in an atomic plane of a lattice. The amplitudes of these waves can be parallel, *e.g.* longitudinal, or perpendicular, *e.g.* transversal, to the phonon propagation wavevector $\vec{k}$. In a simplified picture, the atoms in a plane are moving in phase in acoustic modes, whereas in optical modes the atoms are moving out of phase. A crystal with N atoms in the unit cell will have 3 acoustic modes, from which two are transversal and one is longitudinal, and $(3N-3)$ optical phonon modes, from which 2/3 are transversal and 1/3 are longitudinal. The frequency of an

acoustic mode is zero at the Brillouin zone center, increases linearly in the long wavelength region, $\vec{k} \ll \pi/a$, and approaches a constant at the zone boundary, $\vec{k} = \pm\pi/a$, with the lattice parameter a. Optical modes have a non zero frequency at the zone center and the frequency is typically only slightly wavevector dependent. The dispersion relation gives the relation between the wavevector and the frequency of the phonon modes. The dispersion relation is dependent on the mass of the atoms and the force constants, *i.e.* the bonding of the atoms to each other. Furthermore, the dispersion is dependent on the wavevector direction in the Brillouin zone. In the Brillouin zone are special reciprocal lattice points of high symmetry and the typical presentation of phonon dispersions are between these points. The center of the Brillouin zone, $\vec{k}$=(0,0,0), is denoted by Γ. For example, in a body centered cubic system, there are 3 directions to be consider from Γ towards the Brillouin zone boundaries at $\vec{k}$=(1/2,0,0), labeled by X, at (1/2,1/2,0), labeled by M and at (1/2,1/2,1/2), labeled by R. The dispersion can be experimentally obtained by inelastic neutron scattering on a single crystal, see below and Chapter 4.

The density of phonon states, $g(E)$, denotes the number of phonon modes in an energy interval. The density of phonon states is large, where the slope of the dispersion curve is small. If the slope of the dispersion curve is zero, the derivation with respect to the energy of the density of phonon states has a singularity, which is called Van Hove singularity. The total cross-section weighted density of phonon states can experimentally obtained by inelastic neutron scattering on a polycrystalline sample, see below and Chapter 3 and 5. The partial, *e.g.* element specific, density of phonon states can be obtained by nuclear inelastic scattering, see below and in Chapter 2, 3 and 5. From the density of phonon states, different transport and thermodynamic properties can be deduced, see Chapter 2.

The occupation of the phonon states is temperature dependent and increases with temperature, as more modes get excited. The occupation number of the states, $n(E)$, is given by the Bose function: $n(E) = 1/(1 - \exp(E/(\mathrm{k_B}T)))$, with the phonon energy E. For a harmonic crystal, this is the only temperature dependence of the density of phonon states. For a system with anharmonic effects, *e.g.* thermal expansion, temperature dependence of the elastic constants or phase transitions, the harmonic approximation fails and the density of phonon states is temperature dependent after applying a correction of the Bose factor, see especially Chapter 4.

A. Inelastic Neutron Scattering[38]

In contrast to x-ray scattering by the electrons, the scattering process takes place between the nuclei and the neutron. Thermal neutrons have energies in the same order of magnitude as the excitation energy of phonons. Therefore, inelastic neutron scattering is a standard tool to measure the phonon dispersion and the density of phonon states. The elastic cross section for coherent neutron scattering on the nucleus is $d\sigma/d\Omega = |F(\vec{Q})|^2 = \langle b \rangle^2 |\sum_k \exp(i\vec{Q}\vec{r}_k)|^2$, with the scattering length b. The scattering length is not dependent on the number of electrons of the atom, as for x-rays, and neighboring atoms in the periodic table or even isotopes can have very different scattering lengths. If the studied element has several isotopes or a non zero nuclear spin state, incoherent scattering can occur. In contrast to coherent scattering, the incoherent scattering cross section contains no phase information. Incoherent scattering depends only on the correlation between the positions of the same nucleus at different times and shows therefore no interference effects, whereas coherent scattering depends on the correlation between the positions of all nuclei at different times and interference occurs.

In an inelastic neutron scattering process, the wavevector of the neutron is changed, $|\vec{k_i}| \neq |\vec{k_f}|$, due to the energy transfer between the neutron and the probed sample. The momentum and the energy of the total system have to be conserved and accordingly the following relations are obtained: $\vec{Q} = \vec{k}_i - \vec{k}_f = \vec{G} + \vec{q}$ and $\hbar\omega = (\hbar/(2m_n))^2(\vec{k}_i^2 - \vec{k}_f^2)$, with the phonon wavevector $\vec{q}$ and the mass of a neutron m_n. An inelastic scattering process is illustrated in Fig. 8. The coherent part of the inelastic neutron cross section is dependent on the scattering vector $\vec{Q}$, whereas the incoherent part scatters isotropically at all $\vec{Q}$ and is proportional to the density of phonon states for a cubic Bravais crystal. Some elements do not show significant incoherent scattering. In order to determine a proper density of phonon states of coherent scatterer, the typical approximation is to average over a sufficiently large $\vec{Q}$ range. In the incoherent approximation, the density of phonon states, $g(E)$, can be directly obtained from the inelastic neutron scattering, $S(E)$, by $g(E) = S(E)E/n(E)$, with the Bose factor $n(E)$, as described above.

There are essentially two types of inelastic neutron scattering instruments, the triple-axes spectrometers, typically used to study the phonon dispersion on a single crystal, and the time of flight spectrometers, mostly used to study the density of phonon states on powders. *Triple-axes spectrometer*: The IN12 is a typical triple axis spectrometer, see Fig. 9, and was

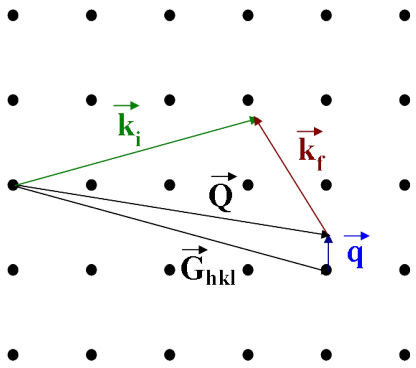

FIG. 8. An inelastic scattering process. $\vec{q}$ denotes the phonon wavevector.

used in this work, see Chapter 4. The IN12 is located at the Institute Laue-Langevin (ILL) research reactor in Grenoble, France. The monochromator, the sample and the analyzer axis can be moved independently in order to cover a large range of energies and of wavevectors. After the neutron beam is monochromized by a single crystal monochromator, typically pyrolitic graphite, it hits the sample and is scattered. The scattered neutrons leave the sample and the analyzer selects neutrons at a defined angle with given energy by Bragg scattering. Only neutrons with a given wavevector are scattered by the analyzer crystal towards the detector. In order to define the orientation of the crystal, a precharacterization measurement is necessary, *e.g.* by Laue diffraction. In order to obtain the phonon mode dispersion, an area around a Bragg reflection is scanned over a phonon wavevector and energy range. For measuring longitudinal modes, $\vec{Q}$ has to be parallel to $\vec{q}$, for measuring transversal modes, $\vec{Q}$ has to be perpendicular to $\vec{q}$. As an example, in order to obtain the acoustic longitudinal mode in [x,x,0] direction, a $\vec{Q}$ scan from (x, x, 0) to (x+1/2, x+1/2, 0) has to be carried out, in an energy range from 0 to ∼8 meV, see also Chapter 4.

Time-of-flight spectrometer: The velocity, v, of a neutron depends on its wavelength, λ, and therefore on the energy of the neutron: $v = h/(m_n\lambda) = \sqrt{2E/m_n}$, with the mass of a neutron m_n. This relation is used to analyze the scattered neutron energy in a time-of-flight spectrometer. A sketch of a typical time-of-flight spectrometer IN6 at the ILL, is shown in Fig. 9. The neutron beam is monochromized by a crystal monochromator. The Fermi chopper defines the zero point of the neutron flight path to the detector: Monochromatic neutron bunches with a fixed time between each bunch hit the polycrystalline sample and are scattered elastically and inelastically. They will be scattered by the sample and will reach the detector in a time, depending of the energy of the neutron. If a neutron annihilates

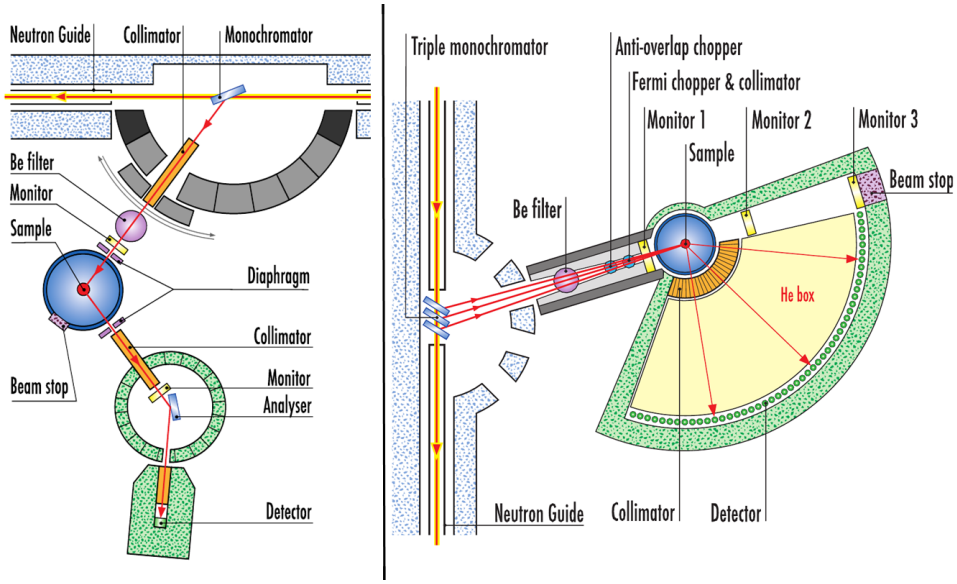

FIG. 9. The triple-axes spectrometer IN12 (left) and the Time-of-Flight spectrometer IN6 (right) from Ref. [39].

a phonon, such that the energy of the neutron is increased, the neutron will reach the detector earlier, than an elastically scattered neutron. If the neutron creates a phonon, the neutron loose some energy and it will be slower than the elastically scattered neutrons. Since the distance between the Fermi chopper and the detector is well defined, the energy of the scattered neutron can be determined. With this technique, the powder averaged $\vec{Q}$ dependence of the energy dependent scattering, $S(Q, E)$, can be obtained. The scattering intensity typically shows a Q^2 dependence in Q, due to the inelastic scattering cross section. By integrating over Q and multiplying with the Bose function, the total, neutron cross section weighted phonon density of states can be determined in the incoherent approximation, see Chapter 3 and 5. Further spectrometers used in this work are the cold neutrons time-of-flight spectrometer FOCUS, Paul Scherrer Institut (PSI), Switzerland, and the wide angular range copper spectrometer, ARCS, at the Spallation Neutron Source (SNS), USA, which have similar setups, however, at ARCS the incident neutron energy is monochromized by Fermi choppers instead of a monochromator crystal.

B. Nuclear Inelastic Scattering[40–42]

This method is based on the Mössbauer effect. The Mössbauer effect describes the recoil-free absorption or emission of a γ-ray by a nucleus in a solid. When an excited nucleus de-excites by emitting a γ-ray typically the nucleus recoils to the opposite direction of the emitted γ-ray. The energy difference between the excited state and the ground state, E_0, of a nucleus at rest is therefore divided into the emitted γ-ray energy E_γ and the recoil energy E_R. The recoil energy is dependent on the mass of the nucleus and the γ-ray energy: $E_R = E_\gamma^2/(2Mc^2)$, with the speed of light c. The difference between the emitted and absorbed γ-ray is $2E_R$ and a resonant absorption process can only take place, if the natural width of the excited state, Γ, is a least twice of the recoil energy: $\Gamma/2E_R > 1$. This condition is not fulfilled for free, unbound, atoms in a gas or liquid and therefore resonant absorption cannot take place in this case. However, if the excited nucleus is bound in a solid and de-excites, in a semi-classical picture the whole lattice will recoil and therefore the recoil energy is not dependent on the mass of the nucleus but on the mass of the whole crystal system. Therefore, the recoil energy is small, $E_\gamma \approx E_0$, and resonant absorption can take place. The Lamb-Mössbauer factor describes the recoilless fraction $f_{LM} = \exp(-k^2\langle u^2\rangle)$, with the wavevector k of the emitted γ-ray and the mean-square displacement $\langle u^2\rangle$. If all atoms are fixed on their equilibrium positions, the f_{LM} would be one. Due to lattice vibrations and zero point motions, the atoms moves and additional states exist between which the transition can take place, see figure 10. This lowers the f_{LM} and by increasing temperature, more phonons are excited and f_{LM} decreases. The f_{LM} is analogous to the Debye-Waller factor in diffraction measurements.

Many Mössbauer isotopes can be studied by the NIS technique, but due to the limits of the available synchrotron radiation energy and adequate monochromators, isotopes with transition energies larger than ∼37 keV (^{121}Sb) were not studied with NIS so far. Furthermore, the lifetime of the excited state has to be long enough in order to separate nuclear fluorescence and prompt scattering by an electronic detection veto, see below. Although it was shown that it is possible to measure NIS with the ^{201}Hg resonance[43], which exhibits a lifetime of 0.9 ns, no further measurements were carried out with this resonance so far. Therefore, ^{125}Te can be regarded as the isotope with the shortest lifetime (1.5 ns) measurable by a standard NIS setup. At resonance energies above 40 keV, a further difficulty arises from

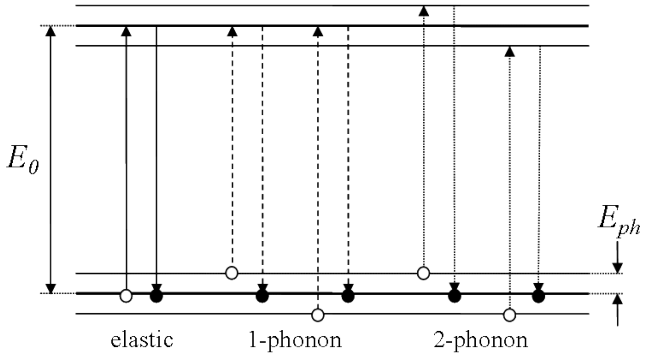

FIG. 10. An elastic nuclear resonant absorption process, solid line, and the incoherent inelastic nuclear resonant scattering of a 1-phonon (dashed line) and a 2-phonon process (dotted line). E_0 and E_{ph} are the resonant transition energy and the phonon energy, respectively.

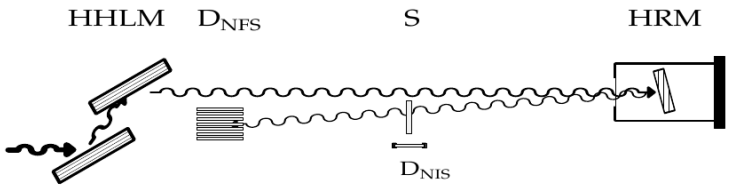

FIG. 11. Simplified setup for the measurement of the nuclear forward and the nuclear inelastic scattering from Ref. [44]. After the high-heat-load monochromator, HHLM, the photon energy bandwidth is in the eV region. The high-resolution monochromator, HRM, reduces the bandwidth to ∼1 meV and the beam is backscattered to the sample, S. The nuclear forward scattering detector, D_{NFS}, and the nuclear inelastic scattering detector, D_{NIS}, detect the forward and inelastic scattering, respectivley.

the large recoil energy, $E_R = E_\gamma^2/(2Mc^2)$, which leads to large multiphonon contributions. While the first inelastic measurements were obtained in 1995 using the ^{57}Fe resonance, the first inelastic measurement on the newest isotopes were in 2006 and 2008 with the ^{121}Sb resonance and with the ^{125}Te resonance[44], respectively. Since then tremendous increase in resolution has been achieved[45] from ∼6 meV to now ∼1 meV. For this work, measurements with the ^{57}Fe, ^{121}Sb and ^{151}Eu resonance were carried out, see Chapter 2, 3 and 5. The incoherent inelastic nuclear resonance scattering process is shown in Fig. 10. If the energy of the incident photon beam includes the transition energy of the nuclear resonance of the studied Mössbauer isotope, photons can be absorbed and the nucleus excites. After some

time, depending on the lifetime of the excited state and the hyperfine structure, the nucleus will decay to the ground state by emitting a photon with the same energy than the initial photon (nuclear forward scattering) or by nuclear fluorescence. If the energy of the incident photon beam is slightly changed to a value near the transition energy, the photons can be absorbed only through simultaneous creation or annihilation of a phonon. Therefore, this method relies essentially on the phonon-assisted nuclear resonance absorption and can be used to directly probe phonon states. In order to measure the phonon spectrum the incident photon energy is tuned in an energy region of typically ± 60 meV around the resonant transition energy, while simultaneously the nuclear fluorescence is detected. A typical spectrum is shown in Fig. 12. The instrumental setup is shown in Fig. 11, in this case for measurements at the ^{121}Sb resonance with a Bragg backscattering monochromator. The synchrotron radiation bunches has to be well separated and the time between two bunches have to be long enough to measure the nuclear fluorescence. After the high-heat-load monochromator, the energy of the photon beam has a bandwidth in the eV range. The high-resolution monochromator monochromizes this beam to a bandwidth of around $\sim$1 meV, which is the required resolution for measuring phonon modes. For measurements with the ^{57}Fe and ^{151}Eu resonance a nested monochromator[41] was used, and for the ^{121}Sb resonance a Bragg backscattering monochromator was used. The tuning of the energy of the latter monochromator is achieved by tuning the temperature of a high quality sapphire single crystal, on which the Bragg backscattering takes place: By tuning the temperature, the distance of the lattice planes changes due to thermal expansion, and therefore the wavelength of the photons, which fulfill Bragg's law, is varied. The requested temperature tuning is in the mK region, see upper scale in Fig. 12, for more details see Ref. [44]. The photon beam hits the sample and the above described transitions can take place. An electronic veto has to be implied, in order to suppress the detection of the prompt Compton, Thomson and electronic fluorescence scattering. The nuclear forward scattering, which is used to determine the instrumental resolution, is detected in the forward scattering and the nuclear inelastic scattering is detected by the inelastic detector. Since nuclear fluorescence is essentially isotropic in all directions, a large angular range has to be covered by the detector and the inelastic detector should be as close as possible to the sample. In order to obtain the density of phonon states from the spectrum, the instrumental resolution has to be taken into account and the one phonon term has to be extracted. After subtraction of the elastic line from the spectrum obtained

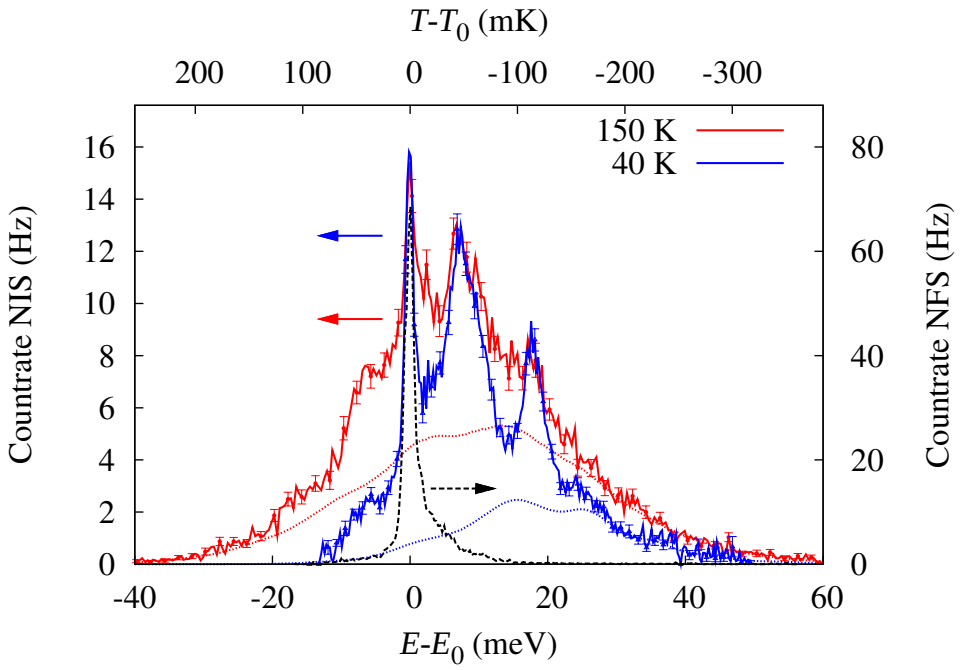

FIG. 12. The nuclear inelastic scattering, NIS, measured on a polycrystalline elemental Sb sample with the ^{121}Sb resonance at 40 K, blue, and 150 K, red, and the nuclear forward scattering, NFS, which was taken as the resolution function, black. The upper x label indicates the temperature change of the monochromator crystal corresponding to the energy transfer $E - E_0$. The dotted lines indicate the multiphonon contribution at 40 K, blue, and 150 K, red.

by the nuclear inelastic scattering detector, the spectrum has to be deconvoluted by the instrumental resolution. Also, two or more phonon transitions can take place, see Fig. 10. The multiphonon contribution is dependent on the Lamb-Mössbauer factor, f_{LM}, and has to be subtracted from the spectrum. As described above, the Lamb-Mössbauer factor is temperature dependent and decreases with temperature, see Fig. 12. For ^{57}Fe, there is typically a much smaller decrease of the Lamb-Mössbauer factor as for ^{121}Sb. Therefore, Fe NIS can be measured at room temperature, but for ^{121}Sb low temperature measurements are preferable, due to the large multiphonon contribution at high temperatures, and the therefore imprecise extraction of the one phonon term.

From the extracted element specific density of phonon states the velocity of sound and the element specific Debye temperature, mean force constant and lattice heat capacity can be obtained[42], see Chapter 2, 3 and 5.

[1] D. M. Rowe, *Thermoelectrics Handbook: Macro to Nano* (Taylor & Francis Group, Boca Raton, 2006).

[2] B. C. Sales, Science **295**, 1248-1249 (2002).

[3] N. W. Ashcroft, and N. D. Mermin, *Solid State Physics* (Thomson Learning, 1976).

[4] H. J. Goldsmid, *Introduction to Thermoelectricity* (Springer-Verlag Berlin Heidelberg, 2010).

[5] G.A. Slack, *CRC 'Handbook of Thermoelectrics'*, 407-440 (CRC Press, 1995).

[6] J. R. Sootsman, D. J. Chung, and M. G. Kanatzidis, Angew. Chem. Int. Ed. **48**, 8616-8639 (2009).

[7] D. M. Rowe, *Modern Thermoelectrics*, (Holt, Rinehart and Winston Ltd., 1983).

[8] N. Wiberg, *Lehrbuch der Anorganischen Chemie* (de Gruyter, Berlin, 1995).

[9] E. S. Toberer *et al.*, Chem. Mater. **22**, 624-634 (2010).

[10] S. M. Kauzlarich S. R. Brown, and G. J. Snyder, Dalton Trans. **21**, 2099-2107 (2007).

[11] J. Y. Chan *et al.*, Chem. Mater. **10**, 3583-3588 (1998).

[12] B.C. Sales *et al.*, Science **272**, 1325-1328 (1996).

[13] G. S. Nolas *et al.*, J. Appl. Phys. **79**, 4002-4008 (1996).

[14] G. S. Nolas, J. L. Cohn, and G. A. Slack, Phys. Rev. B **58**, 164-170 (1998).

[15] D. T. Morelli *et al.*, Phys. Rev. B **56**, 7376 (1997).

[16] B. C. Sales *et al.*, Phys. Rev. B **56**, 15081-15089 (1997).

[17] M. Christensen *et al.*, Nature Materials **7**, 811-815 (2008).

[18] M. M. Koza *et al.*, Nature Materials **7**, 805-810 (2008).

[19] N. R. Dilley *et al.*, Phys. Rev. B **61**, 4608-4614 (2000).

[20] M. D. Hornbostel *et al.*, J. Am. Chem. Soc. **119**, 2665-2668 (1997).

[21] M. Beekman *et al.*, J. Phys.: Condens. Matter **22**, 355401 (2010).

[22] J. Dong, O. F. Sankey, and C. W. Myles, Phys. Rev. L **86**, 2361-2364 (2001).

[23] G. S. Nolas *et al.*, Appl. Phys. Lett. **82**, 910-912 (2003).

[24] R. P. Hermann *et al.*, Phys. Rev. B **72**, 174301 (2005).

[25] B. C. Sales *et al.*, Phys. Rev. B **63**, 245113 (2001).

[26] L. Qiu *et al.*, Phys. Rev. B **70**, 035208 (2004).

[27] S. R. Brown *et al.*, Chem. Mater. **18**, 1873-1877 (2006).

[28] G.A. Slack, *Solid State Physics 34*, edited by H. Ehrenreich, 1-71 (Academic Press, 1979).

[29] *Manual to the Physical Properties Measurement System (PPMS) from Quantum Design.*

[30] A. Migliori *et al.*, PHYSICA B **183**, 1-24 (1993), and A. Migliori, and J. L. Sarrao, *Resonant ultrasound spectroscopy* (Wiley, New York, 1997).

[31] L. Zhang *et al.*, Mater. Sci. Eng. B **170**, 26-31 (2010).

[32] Y. P. Varshni, Phys. Rev. B **2**, 3952-3958 (1970).

[33] V. Keppens *et al.*, Nature **395**, 876-878 (1998).

[34] R. B. Schwarz, and J. F. Vuorinen, J. Alloys Comp. **310**, 243-250 (2000).

[35] C. Kittel, *Einführung in die Festkörperphysik* (R. Oldenbourg Verlag GmbH, München, 1996).

[36] J. Rodriguez-Carvajal, *FULLPROF V (2009)*(Laboratoire Leon Brillouin (CEA-CNRS), France, 2009).

[37] M. T. Dove, *Introduction to Lattice Dynamics* (Cambridge University Press, 1993).

[38] G.L. Squires, *Introduction to the theory of thermal neutron scattering*, (Cambridge University Press, 1978).

[39] *http://www.ill.eu/fileadmin/users_files/Other_Sites/YellowBook2008CDRom/index.htm*

[40] Y.-L. Chen, and D.-P. Yang, *Mössbauer Effect in Lattice Dynamics* (WILEY-VCH Verlag GmbH & Co. KGaA, Weinheim, 2007).

[41] R. Röhlsberger, *Nuclear Condensed Matter Physics with Synchrotron Radiation*, (Springer-Verlag Berlin Heidelberg, 2004).

[42] R. Rüffer, and A. I. Chumakov, Hyp. Interact. **128**, 225-272 (2000).

[43] D. Ishikawa, A. Q. R. Baron, and T. Ishikawa, Phys. Rev. B **72**, 140301(R) (2005).

[44] H. C. Wille *et al.*, Europhys. Lett. **91**, 62001 (2010).

[45] I. Sergueev *et al.*, J. Synch. Rad., submitted (2011).

Chapter 2

Lattice Dynamics in the $FeSb_3$ Skutterudite

Lattice Dynamics in the $FeSb_3$ Skutterudite

A. Möchel,[1,2] I. Sergueev,[3] N. Nguyen,[4] Gary J. Long,[5]
F. Grandjean,[2] D. C. Johnson,[4] and R. P. Hermann[1,2,*]

[1]*Jülich Centre for Neutron Science JCNS and Peter Grünberg Institut PGI, JARA-FIT, Forschungszentrum Jülich GmbH, D-52425 Jülich, Germany*

[2]*Faculté des Sciences, Université de Liège, B-4000 Liège, Belgium*

[3]*European Synchrotron Radiation Facility, F-38043 Grenoble Cedex, France*

[4]*Department of Chemistry and Materials Science Institute, University of Oregon, Eugene, OR 97403, USA*

[5]*Department of Chemistry, Missouri University of Science and Technology, University of Missouri, Rolla, Missouri 65409-0010, USA*

Abstract

Thin films of $FeSb_3$ were characterized by electronic transport, magnetometry, x-ray diffraction, ^{57}Fe and ^{121}Sb nuclear inelastic scattering, and ^{57}Fe Mössbauer spectroscopy. Resistivity and magnetometry measurements reveal semiconducting behavior with a 16.3(4) meV band gap and an effective paramagnetic moment of 0.57(6) μ_B, respectively. A systematic comparison of the lattice dynamics with $CoSb_3$ and $EuFe_4Sb_{12}$ reveals that the $[Fe_4Sb_{12}]$ framework is softer than the $[Co_4Sb_{12}]$ framework, and that the observed softening and the associated lowering of the lattice thermal conductivity in the $R Fe_4Sb_{12}$ filled skutterudites is not only related to the filler but also to the $[Fe_4Sb_{12}]$ framework.

PACS numbers: 63.20.D-, 76.80.+y, 72.20.Pa, 61.05.C-, 65.40.Ba, 65.40.De,

I. INTRODUCTION

Skutterudites are promising thermoelectric materials that have been intensively studied since the 1990s[1–4]. They possess interesting semiconducting properties, notably a large Seebeck coefficient, and a relatively low thermal conductivity that has been ascribed to the dynamics of the filler[5–7]. In particular the lattice dynamics of filled and unfilled skutterudites has been the object of intensive research[8–12]. The semiconducting, magnetic, and thermal properties of the filled $R(Fe,Co)_4Sb_{12}$ skutterudites can be tuned[6,13] by filling the $(Fe,Co)_4Sb_{12}$ framework with monovalent ions, *e.g.* Na^+ and Tl^+, divalent ions, *e.g.* Yb^{2+} and Eu^{2+}, or trivalent ions, *e.g.* La^{3+} and Ce^{3+}. However, only a limited degree of filling can be achieved[6,13,14] in $CoSb_3$. In order to achieve larger degrees of filling either Co must be substituted by Fe or a synthesis involving ball milling and subsequent hot pressing must be used[15].

Because there is no bulk synthesis procedure, the influence of filling the $FeSb_3$ structure on its lattice dynamics has been studied by different approaches. The direct comparison with the lattice dynamics of the $[Fe_4Sb_{12}]$ polyanion is not possible, thus one approach is the comparison[9,10] of the lattice dynamics of the filled structures mentioned above with the related unfilled $CoSb_3$. Another approach is the study of the contribution of the filler R to the density of phonon states (DPS). Density functional theory calculations of the partial density of phonon states have been carried out and compared with experimental data, obtained by inelastic neutron scattering and nuclear inelastic scattering[16,17]. The partial contributions to the DPS can also be investigated by *ab initio* powder-averaged lattice dynamic calculations and a subsequent comparison with inelastic neutron scattering measurements[11].

The synthesis of $FeSb_3$ is however possible by nanoalloying[18,19] and this approach has recently been improved and now yields higher sample purity, but still produces only small amounts in the form of micrometer thick films. Because detailed knowledge of the lattice dynamics in skutterudites is necessary to unravel the mechanisms that yield their low thermal conductivity, characterization methods suitable for thin films have to be used. Although inelastic neutron scattering experiments are in principle feasible, the beamtime required would be prohibitively long because of the small amount of sample. In contrast, nuclear inelastic scattering (NIS) is a method of choice that yields the DPS for selected elements[20] even with small samples. This method has been applied[21] to the ^{57}Fe nuclear resonance for

some time, and has recently been developed[17] for the ^{121}Sb resonance. The resolution for the latter isotope was recently improved[22] to ∼1.3 meV full width at half maximum (FWHM). It is thus possible to fully access the element specific DPS in $FeSb_3$ and to obtain several related quantities[20], such as the mean force constants, the atomic displacement parameters, and the average velocity of sound.

Herein we report both the macroscopic characterization of high purity $FeSb_3$ by resistivity and susceptibility measurements and the microscopic characterization by synchrotron radiation diffraction, ^{57}Fe Mössbauer spectral measurements, and nuclear inelastic scattering by ^{57}Fe and ^{121}Sb. A comparison of these results with the properties of $CoSb_3$ reveals that $FeSb_3$ is significantly softer, an observation that both reveals a combined influence of the filler and the substitution of Fe for Co on the lattice dynamics and hence thermal properties, and provides additional clues to the low thermal conductivity in filled skutterudites.

II. EXPERIMENTAL

The $FeSb_3$ thin films were deposited on Kapton foil at ambient temperature by the elemental modulated reactant method in a custom-built ultra high vacuum, $\approx 10^{-5}$ Pa, deposition system described elsewhere[23]. Fe was deposited by using a 3 kW electron beam gun at a rate of 0.4 Å/s and Sb was deposited by using an effusion cell at a rate of 0.6 Å/s. A computer was used to control the deposition procedure. A quartz crystal monitoring system placed 25 cm above each source was used to control the elemental layer modulation, the deposition rates, the shutter opening time for Fe, and the thickness for Sb. The precursors for the crystallized films were prepared by depositing multiple alternate layers of Fe and Sb until the desired film thickness was obtained. Deposition parameters were determined to yield the appropriate molar stoichiometry of $FeSb_3$. These precursor films were then annealed under a nitrogen atmosphere at 410 K to form $FeSb_3$. With this method, two films of thicknesses of ∼1 and ∼1.5 μm were deposited on a 25 μm thick Kapton substrate. All further measurements were carried out on these two films.

Temperature dependent resistivity and magnetization measurements were carried out between 10 and 300 K on a physical properties measurement system (QD-PPMS) with the resistivity and the vibrating sample magnetometer option. The resistivity was measured on several 1 μm thick samples with 2 by 5 mm^2 lateral dimension with different microcrack

structures, see below. The magnetization measurements were carried out with an applied magnetic induction of 0.25 T on a 80 cm by 3.7 mm long wrapped ribbon of the 1 μm thick film, *i.e.* ∼12.9 mg of $FeSb_3$. Hysteresis measurements have been carried out at 300 K up to 1.5 T in order to assess the presence of impurity phases and the diamagnetic contribution to the susceptibility. The same measurements have been carried out on polycrystalline $CoSb_3$ for comparison. The susceptibility, χ, was calculated from the magnetization by assuming the validity of the low field limit approximation $\chi = M/H$, where M is the magnetization and H the applied field.

Temperature dependent x-ray diffraction measurements were carried out at the 6-ID-D high-energy station at the APS between 10 and 300 K. The x-ray wavelength was 0.124269 nm, the area detector was at 1601 mm from the sample, and silicon (Chempur, 99.999%) was used as an internal standard. The sample contained 10 layers of a ∼1.5 μm thick film of $FeSb_3$ on Kapton foil and, for better thermal coupling to the sample holder, Al foil was placed between each layer. The powder diffraction pattern of $CoSb_3$ was measured under the same conditions. The data was reduced to diffractograms by using Fit2D[24] and analyzed using the Rietveld method[25].

The ^{57}Fe Mössbauer spectra have been measured between 4.2 and 295 K on a constant-acceleration spectrometer that utilized a 295 K rhodium matrix ^{57}Co source and was calibrated at 295 K with α-Fe powder.

The ^{121}Sb NIS by $FeSb_3$ was measured at the ID22N station at the ESRF operating in 16-bunch mode. A resolution of 1.3 meV was reached by using a high resolution backscattering monochromator with the (8 16 $\overline{24}$ 40) reflection of a sapphire single crystal cooled to ∼237 K. The sample containing 6 layers of a ∼1.5 μm thick film of $FeSb_3$ on Kapton foil with Al foil between each layer was cooled to 25 K in order to minimize multiphonon scattering. The ^{121}Sb NIS of $CoSb_3$ and $EuFe_4Sb_{12}$ was measured on powder samples with the same setup and resolution. The 295 K ^{57}Fe NIS on the same $FeSb_3$ sample was measured at the ID18 station at the ESRF operating in 16 bunch mode with a resolution of 0.7 meV.

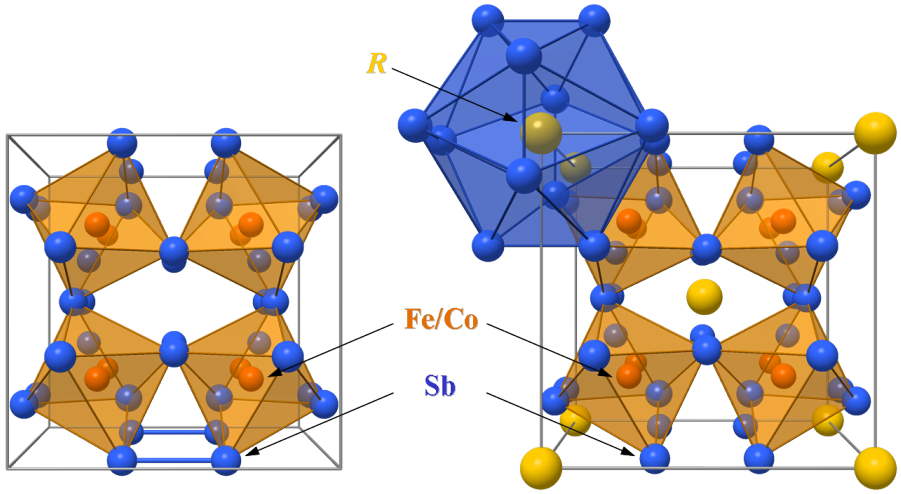

FIG. 1. The structure of unfilled $CoSb_3$ or $FeSb_3$ (left) and filled RFe_4Sb_{12} (right) skutterudite. Co or Fe, Sb, and R are shown in red, blue, and yellow, respectively. The blue rectangle indicates one of the Sb rings, see text.

III. RESULTS AND DISCUSSION

A. Electric transport and magnetism

Above ∼40 K the electrical resistivity, ρ_{el}, of $FeSb_3$ decreases with increasing temperature, see Fig. 2, a decrease that is indicative of semiconducting behavior. A fit of the data in high temperature region, see upper inset in Fig. 2, with[26] $\rho_{el}(T) = A \cdot \exp(E_g/2k_BT)$, where E_g is the energy gap, k_B the Boltzmann constant, T the temperature, and A a proportionality constant, yields an electronic band gap of 16.3(4) meV, a narrower gap than the 50 meV gap obtained by resistivity measurements[26] on lightly p-doped $CoSb_3$. As expected for rather thin films, the microstructure was found to be very important and resistivity measurements were carried out on several samples. The smallest cracks or scratches will increase the resistivity by several orders of magnitude with respect to pristine samples, see the lower inset in Fig. 2. Further, heating the sample above 300 K, not shown, induces additional microstructure and increases the resistivity, because of the differential thermal expansion between Kapton and $FeSb_3$. Atomic force microscopy measurements were carried out to monitor this behavior and to assure that the results in Fig. 2 were obtained on a sample free of cracks at the ∼50 nm level. Such a dependence of the resistivity on the microstructure has also been observed[27] in polycrystalline $CoSb_3$, with reported resistivities of undoped samples between

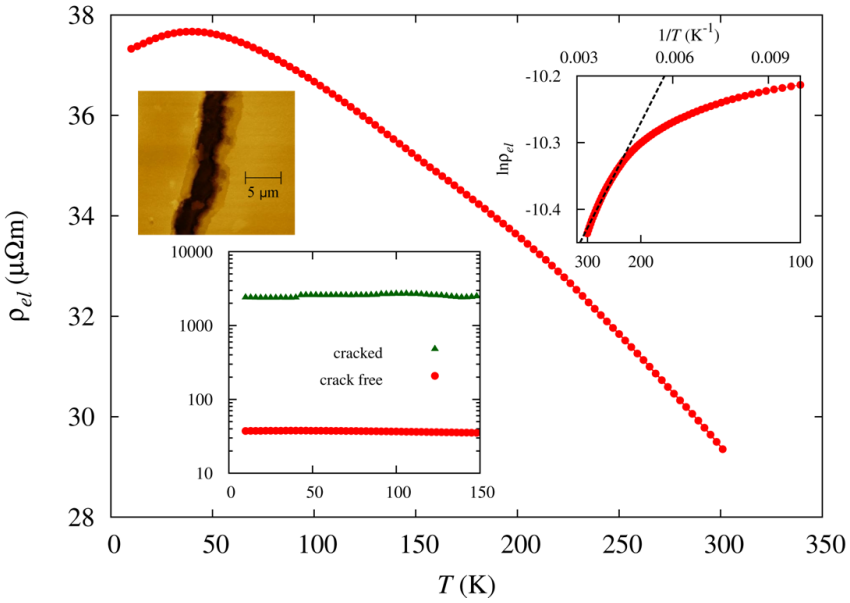

FIG. 2. Electrical resistivity, ρ_{el}, of $FeSb_3$ obtained between 10 and 300 K on a crack free sample, the errors are the size of the data points. The lower left inset shows a comparison between 10 and 150 K of the crack free (red) and a cracked sample (green) on a logarithmic scale. The top right inset shows the fit between 220 and 300 K, see text. The top left shows an atomic force microscopy depth contrast view of a cracked sample.

7 and 1000 $\mu\Omega$m at room temperature[27–33]. The 300 K resistivity of 29.4(1) $\mu\Omega$m observed for crack free $FeSb_3$ is similar to the 37 $\mu\Omega$m of a polycrystalline, sintered, $CoSb_3$ sample[30], which also exhibits the temperature dependence of a typical semiconductor.

The molar susceptibilities, χ_m, of $FeSb_3$ and $CoSb_3$ are shown in Fig. 3. First, the diamagnetic contribution was obtained from the slope of a hysteresis loop measurement at 300 K, see Fig. 4, and is associated with the sample holder, the ion core diamagnetism, and, for the $FeSb_3$ films, to the Kapton substrate. The resulting corrections of χ_m^{dia} were assumed to be temperature independent and were used to obtain the results shown in Fig. 3. Second, the ferromagnetic contribution resulting from a small amount of ferromagnetic impurity in $FeSb_3$ was obtained from the hysteresis loop, see Fig. 4, and corrected for. The magnetization of this impurity is essentially saturated at 0.25 T. Finally, a small correction term, χ_0, amounting to ∼12% of the diamagnetic correction was added to account for imperfections in the correction procedure. Adding this χ_0 immediately yielded paramagnetic Curie-Weiss behavior for $FeSb_3$ between 70 and 300 K. A plot of $1/\chi_m$, see left inset in Fig. 3, yields

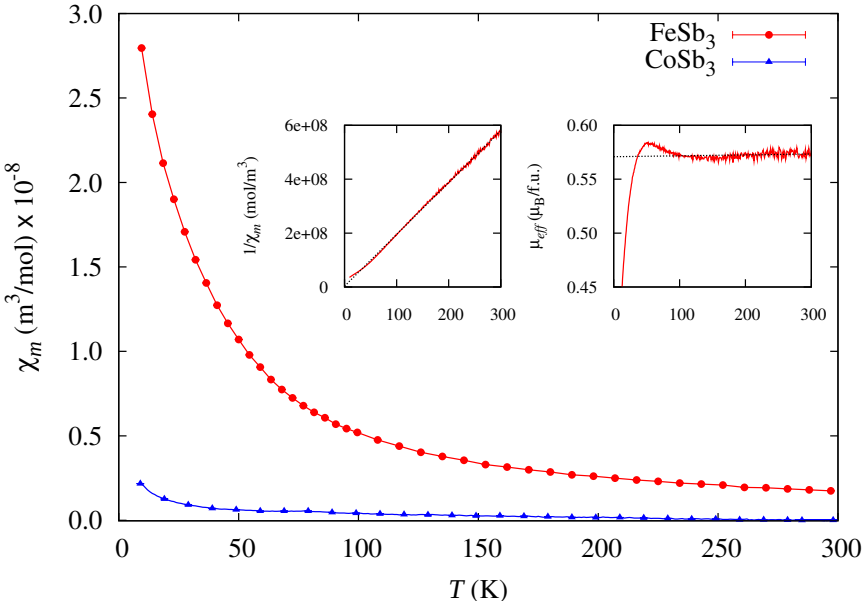

FIG. 3. The molar magnetic susceptibility obtained at 0.25 T between 10 and 300 K for $FeSb_3$ (red) and $CoSb_3$ (blue) after subtraction of both the diamagnetic contribution, calculated from the slope of a hysteresis loop at 300 K shown in Fig. 4, and the ferromagnetic contribution. The errors are the size of the data points. Left inset: the inverse susceptibility of $FeSb_3$. Right inset: the effective moment of $FeSb_3$.

a Curie constant of 0.0414(1) m^3K/mol with a 0 K Curie-Weiss temperature. The right inset of Fig. 3 indicates, that the effective paramagnetic moment of $FeSb_3$ of 0.57(6) μ_B per formula unit, obtained from $\mu_{eff} = 797.8 \cdot \sqrt{\chi_m \cdot T}$, is temperature independent above ~70 K. The same approach was used for $CoSb_3$ and an effective paramagnetic moment of 0.10(6) $\mu_B/f.u.$ was obtained, a value that is compatible with an earlier report[33]. A study of $Co_{1-x}Fe_xSb_3$ with x ranging from 0 to 0.1 has shown, that μ_{eff} increases with increasing Fe content up to a maximum of 1.7 $\mu_B/f.u.$, a value that could correspond[32] to low spin Fe^{3+}. This behavior obviously does not extrapolate to $FeSb_3$, which exhibits a much smaller effective paramagnetic moment.

From the y axis intercept of the magnetic hysteresis loop in Fig. 4 an impurity phase of 0.004(1) atom % was obtained by assuming a typical mean value of 2.2 μ_B per Fe impurity atom at room temperature. The coercive field of ~80 Oe indicates, that the impurity phase is not elemental Fe. For $CoSb_3$ an elemental Co impurity phase of 0.0005(2) atom % was obtained by the same procedure.

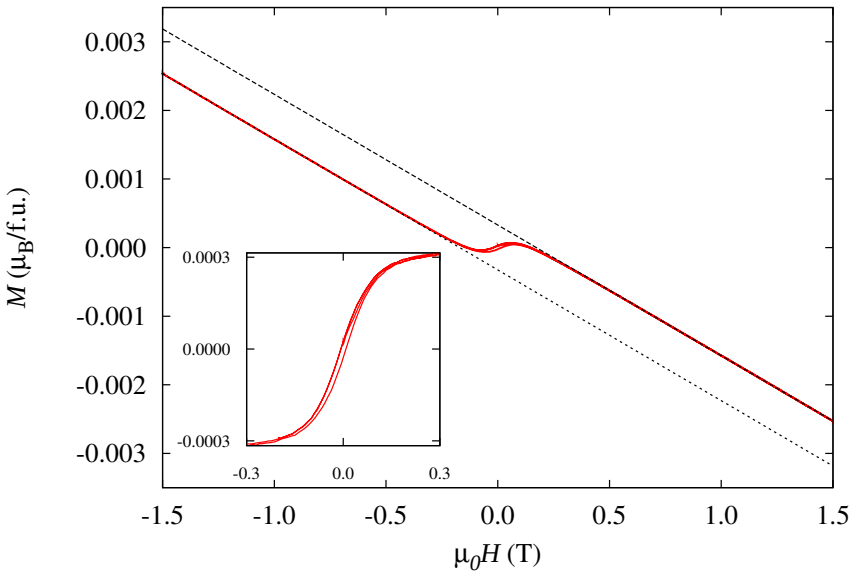

FIG. 4. Hysteresis loop of $FeSb_3$ measured at 300 K. The negative slope is indicative of diamagnetic behavior. The inset shows the hysteresis loop obtained after the diamagnetic correction discussed in the text.

B. X-ray diffraction

X-ray diffraction, see Fig. 5, indicates[18,34], that both $FeSb_3$ and $CoSb_3$ form a cubic lattice with space group $Im\overline{3}$ (number 204) and have the skutterudite structure, see Fig. 1, where Fe or Co and Sb are located on the $8c$ and $24g$ sites, respectively. The inset to Fig. 5 shows the detector image with homogeneous Debye-Scherrer rings that indicate the absence of texture. Apart from the Si internal standard no reflections from a secondary phase or the Al thermalization layers are observed. Because of the large background resulting from the 10 layers of Kapton foil, the Fourier filtering option was used to properly subtract the background. The parameters obtained at 10 and 300 K by Rietveld refinements are given in Table I. The Sb occupation was refined assuming full occupation of the Fe or Co site. The density obtained from the lattice parameters is also given in Table I. A temperature dependent diffraction study on $CoSb_3$ was carried out for comparison and the refinement parameters given in Table I are in good agreement with the literature values[34]. From the refinement of the Sb occupation at 10 K a stoichiometry of $FeSb_{2.88(5)}$ and $CoSb_{2.97(5)}$ has been obtained. The corresponding 0.96(1) Sb occupancy in $FeSb_3$ is however questionable,

see discussion in the Mössbauer spectroscopy part below.

A study of the $Co_{1-x}Fe_xSb_3$ solid solutions, with x between 0 and 0.1, reveals that their lattice parameters increase linearly with increasing Fe content, in agreement with Vegard's law[32]. If we assume, that this linearity holds true for higher Fe content, a lattice parameter of 9.126 Å is expected for $FeSb_3$, a value that is in clear disagreement with the much larger 9.2383(3) Å found herein at 300 K. The thermal expansion calculated from the temperature dependence of the lattice parameters is shown in Fig. 6. In order to reduce noise in this data, especially at low temperatures, the temperature dependence of the lattice parameters was first modeled with a third-order polynomial function, $a_m(T)$, see the fit lines in the top of Fig. 6. The differences between the fitted curve and the data was less than $4 \cdot 10^{-4}$ Å. The thermal expansion coefficient, α, was then obtained from the derivative $\alpha = (da_m(T)/dT)/a_m(300\text{K})$. The thermal expansion coefficient of $CoSb_3$ at 220 K, $8.8{\cdot}10^{-6}$ K^{-1}, is in good agreement with the literature value[35] of $9.1{\cdot}10^{-6}$ K^{-1} as obtained from dilatometry. The thermal expansion of $FeSb_3$ is larger as compared with $CoSb_3$. Under the assumption, that Poisson's ratio for $CoSb_3$ [9], $\nu = 0.22$, is the same for $FeSb_3$, the bulk modulus can be extracted from the sound velocity[36], which can be obtained from NIS, see below. The Grüneisen coefficient[37], $\gamma = 3\alpha BV_m/C_V$, can be obtained by using the thermal expansion coefficient, the bulk modulus, $B = 47.9(1)$ and 83.2(1) GPa for $FeSb_3$ and $CoSb_3$, respectively, the molar volume, V_m, and the heat capacity, C_V, see below. In $FeSb_3$ the resulting γ value of 1.4(1) at 300 K is only slightly larger than the 1.30(5) obtained for $CoSb_3$, because $FeSb_3$ exhibits at the same time a much larger thermal expansion and a much smaller bulk modulus compared to $CoSb_3$.

The refined isotropic mean square displacements, $\langle u^2 \rangle$, for Fe and Sb in $FeSb_3$ are shown in Fig. 7. From the slope of the mean square displacements[38], $d\langle u^2 \rangle/dT = 3\hbar^2/(mk_B\theta_D^2)$, where m is the mass of Sb or Fe, fitted between 100 and 300 K, Debye temperatures, θ_D, of 230(5) and 410(10) K for Sb and Fe, respectively, have been obtained. The average value of the Debye temperature in $FeSb_3$, calculated from $\theta_D^{av} = (3\theta_{D,\text{Sb}} + \theta_{D,\text{Fe/Co}})/4$, is 275(5) K. The mean square displacements of Sb and Co in $CoSb_3$ are also shown in Fig. 7. In $CoSb_3$ the Debye temperatures of 280(10) and 380(30) K for Sb and Co, respectively, have been obtained, and $\theta_D^{av} = 305(15)$ K is larger than in $FeSb_3$; the average value is in good agreement with the literature value[39] of 307 K, obtained by heat capacity, for $CoSb_3$.

Sb is located on a general (0, y, z) position and the y and z positions have been refined.

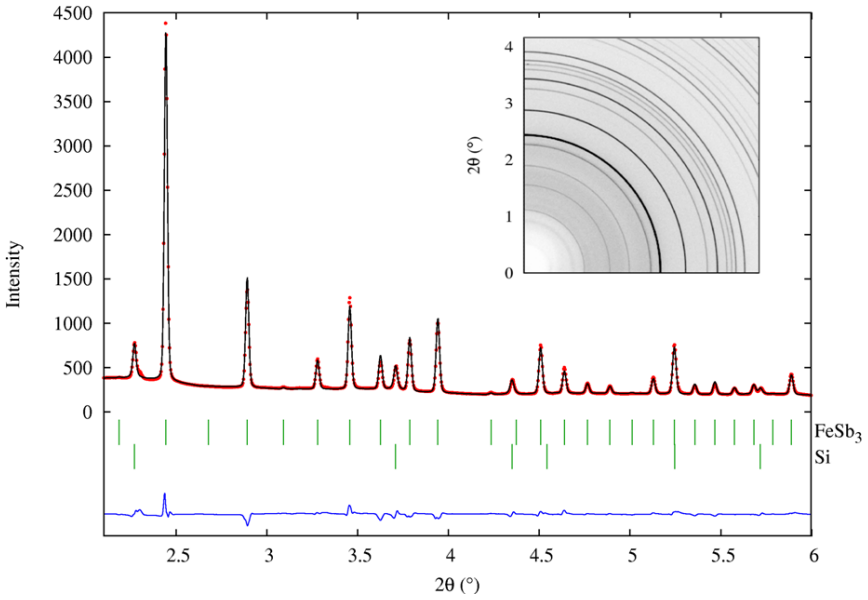

FIG. 5. X-ray diffraction pattern of $FeSb_3$ obtained at 10 K, red dots, the corresponding Rietveld refinement, black line, the difference plot, blue line, and the peak positions for $FeSb_3$ and Si, green ticks. Inset: a quarter of the corresponding detector image.

TABLE I. Rietveld refinement parameters for $FeSb_3$ and $CoSb_3$.

* constrained to the 10 K value.

	$FeSb_3$ (10 K)	$FeSb_3$ (300 K)	$CoSb_3$ (300 K)
Bragg R-factor (%)	7	6	6
R_f (%)	6.5	6.5	5
a (Å)	9.2116(3)	9.2383(3)	9.0320(5)
y Sb	0.3402(2)	0.3399(3)	0.3356(3)
z Sb	0.1578(2)	0.1573(3)	0.1586(3)
Sb occupation	0.96(1)	0.96(1)*	0.99(1)
Density (g/cm^3)	7.157(1)	7.096(1)	7.648(1)

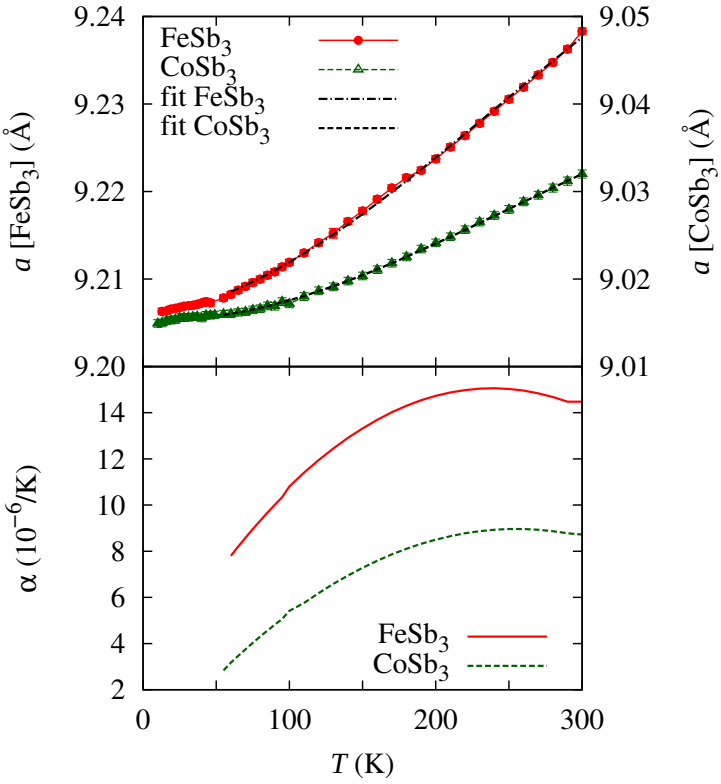

FIG. 6. The temperature dependence of the lattice parameter, a, for $FeSb_3$, in red, and $CoSb_3$, in green, and the corresponding polynomial fit, top. The thermal expansion coefficient, α, of $FeSb_3$ and $CoSb_3$, bottom.

The sum $y + z$ is 0.4972(6) and 0.4942(6) for $FeSb_3$ and $CoSb_3$, respectively. $FeSb_3$ more closely fulfills the Oftedal relation[40], $y + z = 1/2$, which indicates that the rectangular Sb rings, see Fig. 1, are closer to squares in $FeSb_3$ than in $CoSb_3$.

C. Mössbauer spectroscopy

The 4.2 and 295 K ^{57}Fe Mössbauer spectra of the ∼1.5 μm film of $FeSb_3$ are shown in the upper panel of Fig. 8; the spectra obtained for both films and at intermediate temperatures are very similar. In addition to the diffraction measurements, that revealed no crystalline impurity phase, no further amorphous iron bearing impurity is observed. All measured spectra were fitted with a simple symmetric quadrupole doublet with two Lorentzian lineshapes, whose parameters are given in Table II. The Mössbauer spectra show no evidence for a second component related to Fe with missing Sb near neighbors, as would be expected from

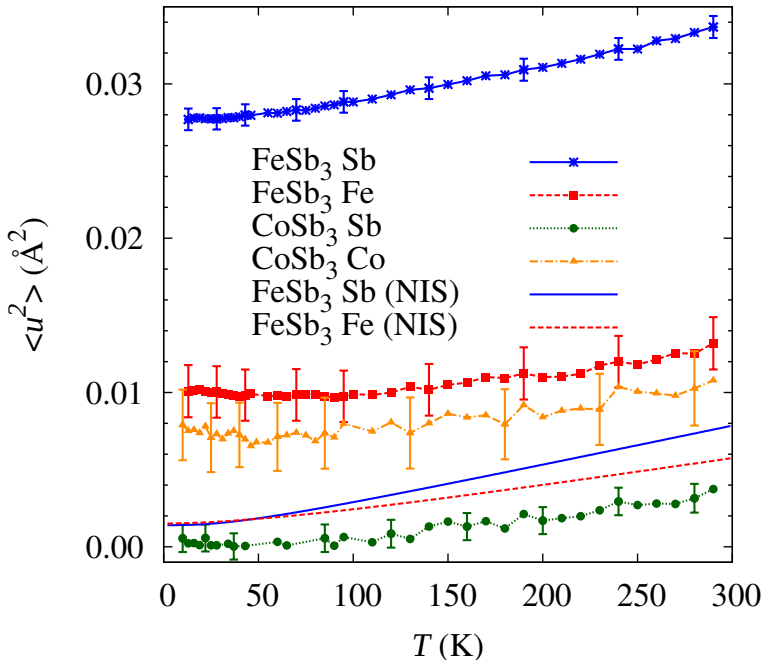

FIG. 7. The mean square displacements, $\langle u^2 \rangle$, obtained from the temperature dependent x-ray diffraction by $FeSb_3$ and $CoSb_3$ and NIS for $FeSb_3$, see below.

the hypothetical partial Sb occupancy seen in the diffraction measurements. The 96(1)% Sb occupancy, see Table I, would imply that more than 20% of the Fe have less than 6 Sb near neighbors, which would be visible in the Mössbauer spectra. The temperature dependence of the isomer shift, δ, quadrupole splitting, ΔE_Q, linewidth, Γ, and the recoil-free fraction, f_{LM}, is shown in the lower portion of Fig. 8. The temperature dependence of δ and f_{LM} have been fit with a Debye model for a solid[41].

The temperature dependence of the isomer shift is well fit with the Debye model[42] for the second-order Doppler shift with a characteristic Mössbauer temperature, θ_M, of 541(10) and 530(10) K for the ∼1.5 and ∼1 μm films, respectively. This temperature is much larger than the Debye temperature, $\theta_{D,\mathrm{Fe}}$, of 350(5) and 373(6) K of the ∼1.5 and ∼1 μm films, respectively, obtained from the temperature dependence of the logarithm of the spectral absorption area, f_{LM}. The latter values are in good agreement with the values obtained herein by other techniques, see Table III. It is known[42] that the two temperatures, θ_M and $\theta_{D,\mathrm{Fe}}$, obtained from the two temperature dependencies are usually different because they depend, for the isomer shift, on $\langle v^2 \rangle$, the mean-square vibrational velocity of the ^{57}Fe,

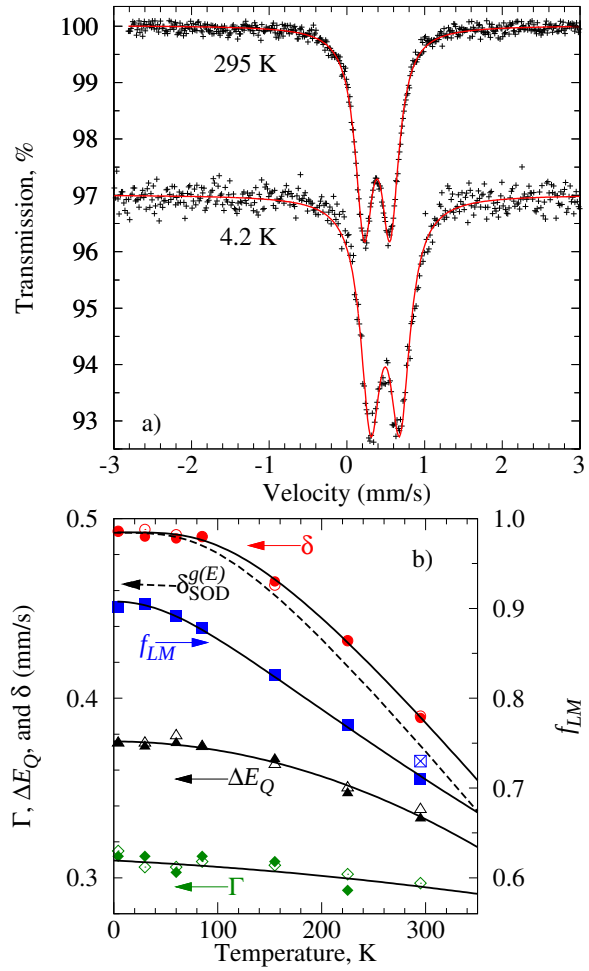

FIG. 8. Upper panel: The Mössbauer spectra of $FeSb_3$ obtained on a 1.5 μm film. Lower panel: The fit parameters obtained from the spectra of the ∼1 and ∼1.5 μm films, open and closed symbols, respectively. The errors are the size of the symbols. The crossed square indicates the f_{LM} obtained directly from the ^{57}Fe NIS at 295 K. The dashed line indicates the second order Doppler shift obtained from the DPS, see text. The lines for the Doppler shift and f_{LM} are Debye model fits[41]. The lines for ΔE_Q and Γ are quadratic polynomial fits given as guide to the eye.

and, for the absorption area, on $\langle u^2 \rangle$, the mean-square atomic displacement of the ^{57}Fe; there is no model independent relationship between these mean square values[42]. However, measurements of the Mössbauer temperatures on various compounds[43] indicate that θ_M is often twice as large as $\theta_{D,\mathrm{Fe}}$, *i.e.* the isomer shift is more sensitive to higher energy phonons.

The Fe DPS of $FeSb_3$, see below, clearly reveals that the Fe vibrations have a strong non-Debye behavior and are dominated by two strong optical modes above 30 meV. Because we have measured the partial DPS, $g(E)$, by ^{57}Fe NIS, see below, we can directly obtain the second order Doppler shift[42] $\delta_{\mathrm{SOD}}^{g(E)} = -\langle v^2 \rangle/(2c)$ from the average kinetic energy[20] $\langle E_{kin} \rangle = 1/2 m_R \langle v^2 \rangle = 3/4 \int_0^\infty coth(E/(2\mathrm{k_B}T)) g(E) E dE$, where m_R is the mass of the resonant nucleus. The obtained temperature dependence of the isomer shift with the second order Doppler correction is shown in Fig. 8, and corresponds to $\theta_M = 440$ K. The difference is thus only partly explained and other corrections such as thermal expansion, which modifies the DPS and therefore $\langle E_{kin} \rangle$, or the influence of charge carrier activation on the isomer shift might be necessary.

D. Nuclear resonance scattering

The nuclear inelastic scattering spectra from the ^{121}Sb NIS measurements in $FeSb_3$, $CoSb_3$, and $EuFe_4Sb_{12}$ are shown in Fig. 9, together with the instrumental functions measured by nuclear forward scattering. The resolution of the instrument was ∼1.3 meV for all measurements. ^{121}Sb NIS measurements on the latter two compounds have been published previously[17] with a resolution of 4.5 meV. The measurements have been repeated, because of the enhanced resolution[22]. After subtraction of the elastic peak, the extraction of the DPS has been performed by the conventional procedure[21,44], *i.e.* the correction of the multiphonon contribution of the Fourier transformation of the inelastic scattering, which was slightly modified in order to take into account the asymmetry of the instrumental function; the data were deconvoluted by the experimental instrumental function and convoluted with a symmetric Gaussian with a FWHM of 1.7 meV, a value slightly larger than the ∼1.3 meV resolution that was chosen in order to avoid unphysical termination ripples in the DPS. The validity of the procedure was confirmed by applying the usual sum rules[45]. The ^{57}Fe NIS spectrum of $FeSb_3$ measured at 295 K is also shown in Fig. 9. The instrumental resolution was 0.7 meV and the DPS was obtained by the conventional procedure[44]. After the mul-

TABLE II. Mössbauer spectral parameters for the $FeSb_3$ films. The errors are estimated to be 0.005 mm/s for the isomer shift, δ, quadrupole splitting, ΔE_Q, and linewidth, Γ, and 0.005 (%ϵ)(mm/s) for the absorption area.

[a]The isomer shifts are given relative to 295 K α-Fe powder.

Thickness (μm)	T (K)	δ (mm/s)[a]	ΔE_Q (mm/s)	Γ (mm/s)	Total Area (%ϵ) (mm/s)
1	295	0.390	0.338	0.297	1.668
	225	0.432	0.350	0.302	1.798
	155	0.463	0.363	0.307	1.917
	85	0.490	0.373	0.309	2.029
	60	0.491	0.379	0.306	2.037
	30	0.494	0.375	0.306	2.040
	4.2	0.493	0.375	0.315	2.070
1.5	295	0.389	0.333	0.276	2.808
	225	0.432	0.347	0.293	3.045
	155	0.465	0.366	0.309	3.266
	85	0.490	0.373	0.312	3.471
	60	0.489	0.375	0.303	3.526
	30	0.490	0.373	0.312	3.577
	4.2	0.493	0.375	0.312	3.564

tiphonon correction, the partial DPS, $g(E)$, were obtained, see Fig. 10, which also shows the ^{57}Fe DPS of $EuFe_4Sb_{12}$ from Ref. 46. The Fe DPS consists of two small broad peaks at ∼7 and 15 meV and a large broad peak around 30 meV. The latter broad peak is split and corresponds to a somewhat softer phonon mode in the $EuFe_4Sb_{12}$ filled skutterudite. The splitting of this peak was also observed in the filled skutterudite $LaFe_4Sb_{12}$ by inelastic neutron scattering measurements[16], and in $CeFe_4Sb_{12}$ by NIS[46]. The low energy portion of the DPS indicates that $FeSb_3$ is softer than $EuFe_4Sb_{12}$ as seen from the large increase in the reduced DPS, $g(E)/E^2$, see insets to Fig. 10. The Sb vibrations mainly appear below 25 meV, but a small contribution of the Sb vibrations is also observed around 30 meV. The

latter part of the DPS is not well resolved due to the multiphonon contributions in the experimental data. By comparing the partial DPS in different compounds, we observe that the Sb DPS in $CoSb_3$ exhibits pronounced features such as gaps at 12 and 21 meV and a well resolved peak at 23 meV. Inelastic neutron scattering measurements have also revealed[16] this better resolution of the individual peaks in $CoSb_3$ as compared with $R Fe_4Sb_{12}$. However, this difference is not directly related to the filling of the skutterudites, because the DPS of $FeSb_3$ shows the same broad features as $EuFe_4Sb_{12}$. The most pronounced difference of the DPS in $FeSb_3$ as compared to other filled and unfilled skutterudites is an overall softening of the phonon modes, which leads to an enhancement of the DPS between 5 and 10 meV. This softening, which is also observed in the Fe DPS in $FeSb_3$ at low energies, see Fig. 10, indicates a lower velocity of sound and might be crucial in determining the thermal conductivity and therefore the thermoelectric properties of skutterudites. In $EuFe_4Sb_{12}$ the essentially single frequency and Einstein like DPS of the Eu filler appears[46] at $\sim$7 meV. The relative hardening of the Sb DPS between $FeSb_3$ and $EuFe_4Sb_{12}$, seen in the lower DPS of $EuFe_4Sb_{12}$ at $\sim$7 meV, might be related to the appearance of this filler mode. Calculations of the lattice dynamics in $FeSb_3$ would thus be highly desirable in order to confirm this hypothesis.

Several thermodynamic and vibrational quantities can be obtained from the DPS[20]. The element specific heat capacity, C_V, can be directly calculated from the DPS. The total heat capacity, C_V^{tot}, of $FeSb_3$, obtained by combining the partial C_V for Fe and Sb obtained from NIS by $C_V^{tot} = 3 \cdot C_V^{\mathrm{Sb}} + C_V^{\mathrm{Fe}}$, are shown in Fig. 11. These values are compared with the total C_V of $CoSb_3$, obtained by combining the partial C_V for Co from calculations[16] and for Sb from NIS measurements, measurements that are in good agreement with the calculation in Ref. 16. Also a macroscopic C_P measurement of $CoSb_3$, carried out with the C_P option of the QD-PPMS that is in excellent agreement with earlier results[39], is also shown. With a Debye fit of the C_V between 2 and 300 K, Debye temperatures for Sb and Fe in $FeSb_3$ of 210(5) and 430(10) K, respectively, have been obtained, values that are in good agreement with those obtained by diffraction, see Table III. From C_V^{tot} for $FeSb_3$, a Debye temperature of 240(10) K has been obtained. The partial C_V of $CoSb_3$ yields Debye temperatures of 250(5) and 410(10) K for Sb and Co, respectively. The total Debye temperature of $CoSb_3$ from the macroscopic measurement is 280(10) K, in good agreement with the θ_D = 285(10) K obtained from the combined experimental ^{121}Sb NIS C_V and the theoretical Co C_V.

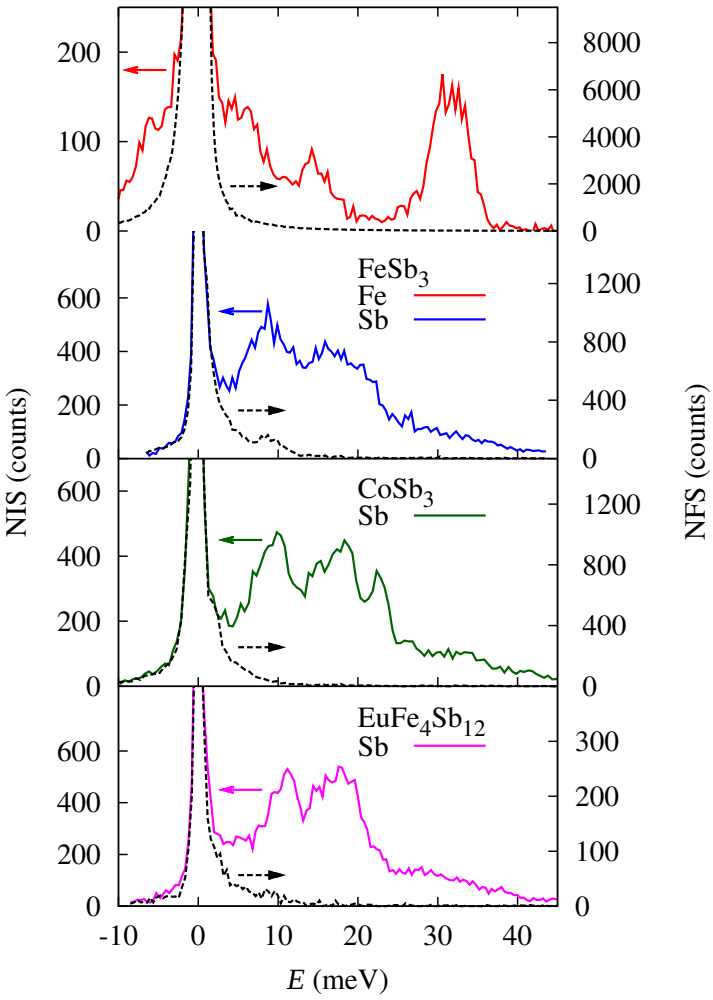

FIG. 9. The nuclear inelastic scattering, NIS, spectra and the instrumental functions, dashed lines, measured by nuclear forward scattering, NFS, obtained with the ^{57}Fe resonance of $FeSb_3$, top, and with the ^{121}Sb resonance of $FeSb_3$, $CoSb_3$ and $EuFe_4Sb_{12}$, bottom.

From the Debye level, $\lim_{E\to 0}(g(E)/E^2)$, obtained from the low energy modes in the reduced DPS, see the insets to Fig. 10, the average velocity of sound, v_s, of 2390(10) and 2790(10) m/s for $FeSb_3$ and $EuFe_4Sb_{12}$, respectively, was obtained from the ^{57}Fe NIS by using[47]

$$\lim_{E\to 0}(g(E)/E^2) = \frac{m_R}{2\pi^2\rho\hbar^3 v_s^3} \quad (1)$$

where ρ is the density of the material and m_R the mass of the resonant nucleus. These velocities of sound are consistent with the Sb Debye level in $FeSb_3$ and $EuFe_4Sb_{12}$, as indicated by the dashed lines in the insets to Fig. 10, see also Table III. For $CoSb_3$ a v_s of 2600(100) m/s is obtained from the Debye level, in fair agreement with the literature value[28] of 2930 m/s.

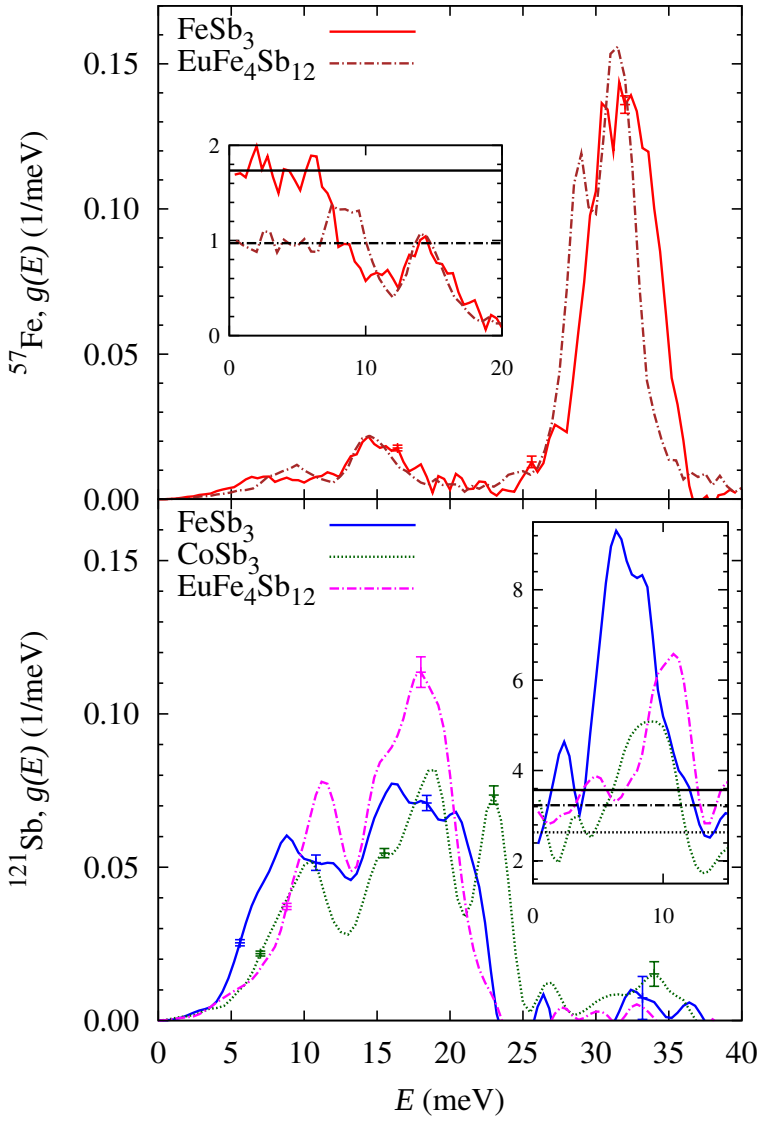

FIG. 10. Comparison of the DPS measured with the ^{57}Fe resonance at 300 K for $FeSb_3$ and $EuFe_4Sb_{12}$, top, and with the ^{121}Sb resonance at 25 K for $FeSb_3$, $CoSb_3$, and $EuFe_4Sb_{12}$, bottom. The insets show the reduced partial DPS, $g(E)/(E^2)$, in units of $10^{-4}/\mathrm{meV}^3$ and the low energy fit, between 0 and 4 meV, for the Debye levels, indicated by the same type of lines. The differences in the Debye levels for Fe and Sb in $FeSb_3$ and $EuFe_4Sb_{12}$ are due to the different masses of the elements, see Eq. 1.

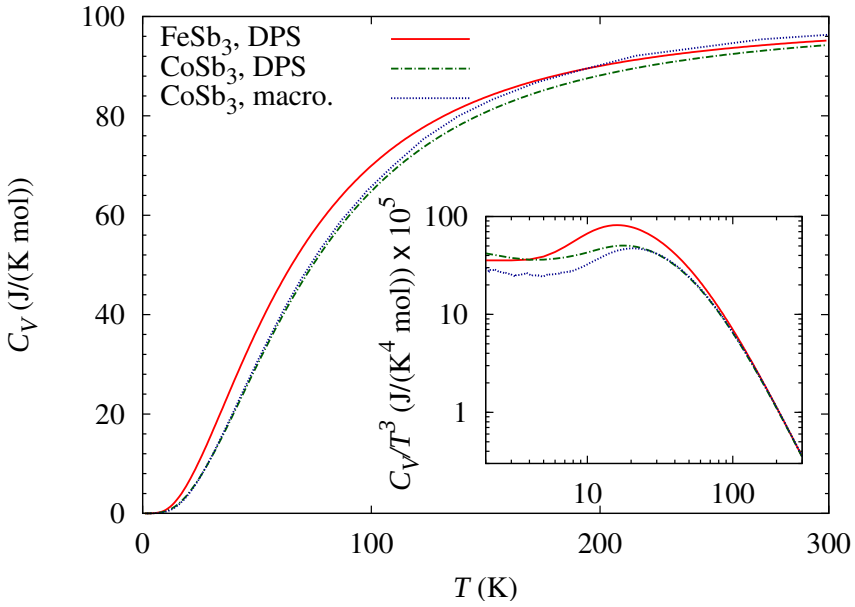

FIG. 11. A comparison of the total heat capacity, calculated from the DPS of $FeSb_3$, red, the total heat capacity, calculated from the DPS and theoretical calculations for $CoSb_3$, green, and the macroscopic measured heat capacity of $CoSb_3$, blue.

The large error arises from the imprecision in the Debye level obtained only from the ^{121}Sb NIS. By using the low temperature Debye approximation, $v_s = (k_B\theta_D)/(\hbar(6\pi^2 N)^{1/3})$, with the density of atoms N, the low temperature $\theta_D^{LT} = 245(5)$ K is obtained for $FeSb_3$, a value significantly lower than $\theta_D^{LT} = 307$ K reported for $CoSb_3$ [39].

The Lamb-Mössbauer factor, f_{LM}, obtained from NIS provides access to the atomic mean square displacements, $\langle u^2\rangle = -ln(f_{LM})/k^2$, where k is the incident wavevector[20]. In $FeSb_3$ the f_{LM}^{Sb} is 0.58(1) and $\langle u^2\rangle$ is 0.0015(5) Å^2 for Sb at 25 K and f_{LM}^{Fe} is 0.733(5) and $\langle u^2\rangle$ is 0.0057(4) Å^2 for Fe at 295 K. These values are much smaller than the $\langle u^2\rangle$ values obtained by diffraction, see Fig. 7. Note that the displacement parameter obtained by NIS is a purely incoherent one particle displacement and is not affected by the site occupation or disorder as the $\langle u^2\rangle$ values obtained from diffraction sometimes are affected. The temperature dependence of $\langle u^2\rangle$ obtained from the DPS[20], see Fig. 7, is in agreement with the temperature dependence of $\langle u^2\rangle$ obtained by diffraction, apart from an additive constant, which reflects a static displacement, or a site disorder, or an incomplete site occupation. The element specific Debye temperatures can also be calculated directly from $g(E)$ with the expression

$\theta_D^2 = 3/({k_B}^2 \int_0^\infty g(E)dE/E^2)$ obtained in the high temperature limit, see Ref. [20]. For $FeSb_3$ Debye temperatures of 210(10) K for Sb and 370(5) K for Fe were obtained; the average value of 255(5) K is in agreement with 245(5) and 240(10) K obtained from sound velocity and C_V, respectively. The element specific Debye temperature in $CoSb_3$ was obtained from the measured ^{121}Sb DPS, 245(5) K, and from the theoretical Co DPS[16], 360(10) K. In order to provide an easy comparison between the results of the different methods, we give a summary of all the Debye temperatures in Table III. Arguably, the Debye temperature is a crude approximation, but allows straightforward comparison. In essence, we observe that the Sb sublattice is systematically softer in $FeSb_3$, whereas the Fe sublattice in $FeSb_3$ is harder than the Co sublattice in $CoSb_3$.

The DPS obtained from NIS also directly yields[20] the element specific mean force constants, $F^m = m_R/\hbar \int_0^\infty g(E)E^2dE$. The mean force constant of 160(10) N/m for Sb in $CoSb_3$ is larger than the values of 105(5) and 100(10) N/m observed for $FeSb_3$ and $EuFe_4Sb_{12}$, respectively, because the high energy optical phonon modes of the filled structure are similar to $FeSb_3$, whereas in $CoSb_3$ they have a larger energy. The Sb force constant in $CoSb_3$ deviates from the literature value of 117 N/m, obtained from earlier NIS measurements[17] and 119 N/m, the mean force constant of Sb obtained from calculations[16]. This deviation can be ascribed essentially to the better resolution and more precise energy calibration available herein[22]. Thus, the good agreement obtained earlier[16,17] is not confirmed herein and the experimental mean force constant in $CoSb_3$ appears to be larger than the calculated value. The Sb mean force constant for $EuFe_4Sb_{12}$ is in good agreement with the F^m obtained from previous NIS measurements[17]. This indicates, that by filling $FeSb_3$ with Eu, the average Sb binding does not change. Further, $CoSb_3$ has very different Sb lattice dynamics and thus is not an ideal compound for investigating the influence of filling upon the lattice dynamics of the RFe_4Sb_{12} compounds. In $FeSb_3$ the Fe mean force constant is 186(1) N/m, a value close to the value of 190(4) N/m in $EuFe_4Sb_{12}$. The calculated mean force constant[16] for Co in $CoSb_3$ of 176 N/m is slightly smaller, indicating a softer Co binding in the $[Co_4Sb_{12}]$ framework as compared to the Fe binding in the $[Fe_4Sb_{12}]$ framework.

TABLE III. Summary of the Debye temperatures and the sound velocities in $FeSb_3$ and $CoSb_3$ obtained by different techniques.
a) obtained from $\theta_D^{av} = (3 \cdot \theta_{D,\mathrm{Sb}} + \theta_{D,\mathrm{Fe/Co}})/4$, *b*) obtained from reference [16], *c*) from reference [39], *d*) from reference [28]

Technique	$FeSb_3$			$CoSb_3$		
	$\theta_{D,\mathrm{Sb}}$, K	$\theta_{D,\mathrm{Fe}}$, K	θ_D^{av}, K	$\theta_{D,\mathrm{Sb}}$, K	$\theta_{D,\mathrm{Co}}$, K	θ_D^{av}, K
$\langle u^2 \rangle$, XRD	230(5)	410(10)	275(5)[a]	280(10)	380(30)	305(15)[a]
Mössbauer spectral area 1.5 μm	-	350(5)	-	-	-	-
Heat capacity DPS	210(5)	430(10)	240(10)	250(5)	410(10)[b]	285(10)
Heat capacity macroscopic	-	-	-	-	-	280(10)
DPS	210(10)	370(5)	255(5)[a]	245(5)	360(10)[b]	270(10)[a]
θ_D form v_s	-	-	245(5)	-	-	307[c]
	$v_{s,\mathrm{Sb}}$, m/s	$v_{s,\mathrm{Fe}}$, m/s	v_s^{av}, m/s	$v_{s,\mathrm{Sb}}$, m/s	$v_{s,\mathrm{Co}}$, m/s	v_s^{av}, m/s
NIS, Debye level	2400(100)	2390(10)	-	2600(100)	-	-
Pulse echo	-	-	-	-	-	2930[d]

IV. CONCLUSION

The magnetic and electric properties of $FeSb_3$ reveal semiconducting and paramagnetic behavior similar to $CoSb_3$, with however a larger effective paramagnetic moment. X-ray diffraction and Mössbauer spectral measurements reveal that the sample is single phase. Measurements of the lattice dynamics and the related quantities show that the Sb binding in $FeSb_3$ is significantly softer than in $CoSb_3$, whereas the Fe sublattice in $FeSb_3$ is harder compared to the Co sublattice in $CoSb_3$. The softening of the low energy modes likely has a large influence on the thermal conductivity and thus favorably impacts the thermoelectric properties in $FeSb_3$. By filling the $[Fe_4Sb_{12}]$ framework, the low energy optical phonon modes, which have mainly Sb character, shift to larger energies. The lattice dynamics in filled skutterudites depends both on the framework and the filler and therefore the $[Co_4Sb_{12}]$ framework is not ideal to study the influence of the filler on the lattice dynamics in RFe_4Sb_{12} skutterudites. It appears that for skutterudites, as was also suggested for clathrates[48], the role of the framework on the lattice dynamics should be revisited.

ACKNOWLEDGMENTS

We thank Dr. H.-C. Wille and Mr. D. Bessas for their support during the NIS measurements and Dr. J.C. Feldman for making his calculation data[16] available. We thank Dr. B.C. Sales for providing the $CoSb_3$ and $EuFe_4Sb_{12}$ samples[17]. The European Synchrotron Radiation Facility and the Advanced Photon Source are acknowledged for provision of synchrotron radiation beam time at the nuclear resonance station ID18 and ID22N and the high energy station 6-ID-D, respectively. RH acknowledges support from the Helmholtz-University Young Investigator Group 'Lattices Dynamics in Emerging Functional Materials'. FG acknowledges the financial support of the Fonds National de la Recherche Scientifique, Belgium (grants 9.456595 and 1.5.064.05). The research at the University of Oregon was funded by National Science Foundation under grant DMR 0907049 and supported in part by ONR Grant No. N00014-07-1-0358 and by the Army Research Laboratory under agreement number W911NF-07-2-0083.

---

* r.hermann@fz-juelich.de

[1] J. P. Fleurial *et al.*, Thirteenth international conference on thermoelectrics, AIP Conference proceedings **316**, 40-44 (1995).

[2] B. C. Sales *et al.*, Phys. Rev. B **56**, 15081-15089 (1997).

[3] G. S. Nolas, D. T. Morelli, and T. M. Tritt, Annu. Rev. Mater. Sci. **29**, 89-116 (1999).

[4] C. Uher, Semiconductors and Semimetals **69**, 139-253 (2001).

[5] G. S. Nolas *et al.*, J. Appl. Phys. **79**, 4002-4008 (1995).

[6] G. S. Nolas, J. L. Cohn, and G. A. Slack, Phys. Rev. B **58**, 164-170 (1998).

[7] G. P. Meisner *et al.*, Phys. Rev. Lett. **80**, 3551-3554 (1998).

[8] J. L. Feldman, and D. J. Singh, Phys. Rev. B **53**, 6273-6282 (1996).

[9] V. Keppens *et al.*, Nature **395**, 876-878 (1998).

[10] R. P. Hermann *et al.*, Phys. Rev. Lett. **90**, 135505 (2003).

[11] M. M. Koza *et al.*, Nature Materials **7**, 805-810 (2008).

[12] M. Rotter *et al.*, Phys. Rev. B **77**, 144301 (2008).

[13] B. C. Sales, B. C. Chakoumakos, and D. Mandrus, Phys. Rev. B **61**, 2475-2481 (2000).

[14] C. Uher, *Thermoelectrics Handbook: Macro to nano* (Taylor & Francis Group, LLC, 2006).

[15] J. Yang *et al.*, Phys. Rev. B **80**, 115329 (2009).

[16] J. L. Feldman *et al.*, Phys. Rev. B **73**, 014306 (2006).

[17] H. C. Wille *et al.*, Phys. Rev. B **76**, 140301(R) (2007).

[18] M. D. Hornbostel *et al.*, J. Am. Chem. Soc. **119**, 2665-2668 (1997).

[19] J. R. Williams, M. B. Johnson, and D. C. Johnson, J. Am. Chem. Soc. **123**, 1645-1649 (2001).

[20] R. Rüffer, and A. I. Chumakov, Hyp. Interact. **128**, 225-272 (2000).

[21] W. Sturhahn *et al.*, Phys. Rev. Lett. **74**, 3832-3835 (1995).

[22] I. Sergueev *et al.*, J. Synch. Rad., under review (2011).

[23] M. Noh, J. Thiel, and D. C. Johnson, Science **270**, 1181-1184 (1995).

[24] A. P. Hammersley, *ESRF Internal Report*, **ESRF97HA02T**, 'FIT2D: An Introduction and Overview', (1997).

[25] J. Rodriguez-Carvajal, *FULLPROF V (2009)*(Laboratoire Leon Brillouin (CEA-CNRS), France, 2009).

[26] D. Mandrus *et al.*, Phys. Rev. B **52**, 4926-4931 (1995).

[27] H. Anno *et al.*, J. Appl. Phys. **83**, 5270-5276 (1998).

[28] T. Caillat, A. Borshchevsky, and J. P. Fleurial, J. Appl. Phys. **80**, 4442-4449 (1996).

[29] L. D. Chen *et al.*, J. Appl. Phys. **90**, 1864 (2001).

[30] M. Puyet *et al.*, Phys. Rev. B **73**, 035126 (2006).

[31] A. L. E. Smalley, S. Kim, and D. C. Johnson, Chem. Mater. **15**, 3847-3851 (2003).

[32] J. Yang *et al.*, Phys. Rev. B **63**, 014410 (2000).

[33] J. Yang, M. G. Endres, and G. P. Meisner, Phys. Rev. B **66**, 014436 (2002).

[34] T. Rosenqvist, Acta Metallurgica **1**, 761-763 (1953).

[35] G. Rogl *et al.*, J. Appl. Phys. **107**, 043507 (2010).

[36] L. Zhang *et al.*, Mat. Sci. Eng. B **170**, 26-31 (2010).

[37] D. T. Morelli, V. Jovovic, and J. P. Heremans, Phys. Rev. Lett. **101**, 035901 (2008).

[38] B. T. M. Willis and A.W. Pryor, *Thermal Vibrations in Crystallography* (Cambridge University Press, 1975).

[39] R. P. Hermann, F. Grandjean, and G. J. Long, Am. J. Phys. **73**, 110-118 (2005).

[40] B. C. Chakoumakos, and B. C. Sales, J. Alloys Compd. **407**, 87-93 (2006).

[41] R. H. Herber in *Chemical Mössbauer Spectroscopy*, edited by R. H. Herber, p.199 (Plenum Press New York, 1984).

[42] G. K. Shenoy and F. E. Wagner, *Mössbauer Isomer Shifts*, p.49 (North-Holland, Amsterdam, 1978).

[43] T. Owen *et al.*, Inorg. Chem. **47**, 8704-8713 (2008).

[44] V. G. Kohn, and A. I. Chumakov, Hyp. Interact. **125**, 205-221 (2000).

[45] H. J. Lipkin, Phys. Rev. B **52**, 10073 (1995).

[46] G. J. Long *et al.*, Phys. Rev. B **71**, 140302 (2005).

[47] M. Y. Hu *et al.*, Phys. Rev. B **67**, 094304 (2003).

[48] M. Christensen *et al.*, J. Am. Chem. Soc. **128**, 15657-15665 (2006).

Conclusions and Outlook

The lattice dynamics in thermoelectric Zintl phases were studied by inelastic neutron scattering, nuclear inelastic scattering and several macroscopic techniques. Combining the results obtained by these methods, a detailed insight into the lattice dynamics and the different mechanisms which lead to the low thermal conductivity in thermoelectric Zintl phases was obtained. The knowledge of these thermal conductivity reduction mechanisms will prove useful in order to search for and enhance new efficient thermoelectric materials. The main mechanisms in the studied Zintl phases are the reduction of the phonon lifetime by the filler, the reduction of the phonon velocity by the filler or a low velocity of sound, and the reduction of the effective heat capacity contribution due to a complex crystal structure.

It was shown, that the skutterudite $FeSb_3$ is significantly softer than the isostructural compound $CoSb_3$. Thus, beside the reduction of the thermal conductivity by the filler, the low thermal conductivity in the filled skutterudite $R Fe_4Sb_{12}$ is also related to the soft $[Fe_4Sb_{12}]$ framework. Furthermore, it was shown, that the lattice dynamics of the $[Fe_4Sb_{12}]$ framework is only slightly affected by filling the structure.
Several mechanisms are responsible for the low thermal conductivity in Ga-Ge clathrates. The reduction of the heat capacity contribution to the thermal conductivity due to the large unit cell of the clathrate structure is one additional mechanism next to the small phonon lifetime and the low phonon group velocity, which are both related to the guest atoms. Furthermore, the predicted avoided crossing in Ga-Ge clathrates was modeled and the influence on the thermal conductivity was investigated. This study reveals, that an avoided crossing could lower the thermal conductivity by up to 30%.
The scattering experiments reveal that in the Zintl phase $Yb_{14}MnSb_{11}$ all phonon modes have energies below 25 meV, which is in agreement with the low Debye temperature. The low mean force constants, and the related low velocity of sound, are one reason for the low thermal conductivity in $Yb_{14}MnSb_{11}$. Furthermore, $Yb_{14}MnSb_{11}$ has a rather large unit cell. Therefore the acoustic modes involve a small fraction of the heat capacity and contribute less efficiently to the thermal conductivity.

Several questions are opened for further investigations:

First, it was shown that the lattice dynamics in RFe$_4$Sb12 skutterudites depend both on the [Fe$_4$Sb$_{12}$] framework and on the filler and the lattice dynamics in the [Fe$_4$Sb$_{12}$] framework changes only slightly when filling the structure. Thus, the influence of the filler and the framework to the lattice dynamics and the thermal conductivity should be revisited.

Second, further studies on the change of the Yb valence state in YbFe$_4$Sb$_{12}$ with the temperature should be carried out and the influence of the related anomalous softening in the elastic constants and the rearrangement of the spectral weight of the Yb phonon states to the thermoelectric properties should be investigated and modeled quantitatively.

Third, this study reveals, that in complex crystal structures the reduction of the heat capacity contribution to the thermal conductivity is an important mechanism for the low thermal conductivity. In order to clarify this reduction both theoretical calculations and further experimental studies of the phonon dispersion have to be carried out.

Fourth, in order to reveal, if an avoided crossing takes place in Ga-Ge clathrates, more theoretical calculations are required. In particular a quantitative modeling of the inelastic neutron scattering with the dynamical structure factor will bring deeper insight into the lattice dynamics and the mechanisms which lead to the low thermal conductivity in Ga-Ge clathrates.

Vita

Anne Möchel was born on the 27th August 1982 in Bremerhaven, Germany. She received her Abitur, German university entrance qualification, at the Schulzentrum Bürgermeister Smidt in Bremerhaven, Germany, in 2002. She received her diploma in Physics from the University of Bonn in 2008. She carried out her doctoral research at the Forschungszentrum Jülich and the University of Liège under the supervision of Dr. Raphaël Hermann.

Publications and submitted or prepared manuscripts:

1. M. Beekman, R. P. Hermann, A. Möchel, F. Juranyi, and G. S. Nolas, **A study of low-energy guest phonon modes in clathrate-II Na_xSi_{136} (x = 3, 23, and 24)**, *J. Phys.: Condens. Matter* **22**, 355401 (2010).

2. H.-C. Wille, R. P. Hermann, I. Sergueev, U. Pelzer, A. Möchel, T. Claudio, J. Perßon, R. Rüffer, A. Said, and Yu. V. Shvyd'ko, **Nuclear forward and inelastic spectroscopy on ^{125}Te and $Sb_2{}^{125}Te_3$**, *Europhys. Lett.* **91**, 62001 (2010).

3. A. Möchel, I. Sergueev, N. Nguyen, Gary J. Long, F. Grandjean, D. C. Johnson, and R. P. Hermann, **Lattice Dynamics in the $FeSb_3$ Skutterudite**, submitted to *Phys. Rev. B*, March 2011.

4. J. Burghaus, M. Sougrati, A. Möchel, A. Houben, R. P. Hermann, and R. Dronskowski, **Local ordering and magnetism in $Ga_{0.9}Fe_{3.1}N$**, submitted to *Phys. Chem. Chem. Phys.*, April 2011.

5. M. S. Diakhate, R. P. Hermann, A. Möchel, I. Sergueev, M. Søndergaard, M. Christensen and M. J. Verstraete, **Thermodynamic, thermoelectric and magnetic properties of $FeSb_2$: A combined first principles and experimental study**, submitted to *Phys. Rev. B*, May 2011.

6. A. Möchel, I. Sergueev, H.-C. Wille, F. Juranyi, H. Schober, W. Schweika, S. R. Brown, S. M. Kauzlarich, and R. P. Hermann, **Lattice dynamics in the thermoelectric Zintl compound $Yb_{14}MnSb_{11}$**, to be submitted to *Phys. Rev. B*, May 2011.

7. A. Möchel, I. Sergueev, H.-C. Wille, J. Voigt, M. Prager, M. B. Stone, B. C. Sales, Z. Guguchia, A. Shengelaya, V. Keppens, and R. P. Hermann, **Lattice dynamics and anomalous softening in the $YbFe_4Sb_{12}$ skutterudite**, to be submitted to *Phys. Rev. B*, May 2011.

8. A. Möchel, W. Schweika, K. Schmalzl, B. C. Sales, and R. P. Hermann, **Experimental study of the phonon dispersion in the $Sr_8Ga_{16}Ge_{30}$ clathrate**, to be submitted to *New Journ. Phys.*, June 2011.
